JACS
JOURNAL OF THE AMERICAN CHEMICAL SOCIETY
pubs.acs.org/JACS
Perspective

Seeing Ligands on Nanoclusters and in Their Assemblies by X-ray Crystallography: Atomically Precise Nanochemistry and Beyond

Yingwei Li and Rongchao Jin*

Cite This: J. Am. Chem. Soc. 2020, 142, 13627−13644
Read Online
ACCESS | Metrics & More | Article Recommendations

ABSTRACT: Ligands are of tremendous importance for colloidal nanoparticles (NPs) in terms of surface protection, size and shape control, tailoring properties, self-assembly, and applications. However, it is very challenging to obtain unambiguous information on the ligands and their interactions and patterning on NPs. The recent advent of atomically precise nanochemistry has opened new horizons. One can now see ligands with atomic resolution and understand their behavior on the surface of ultrasmall NPs (1−3 nm) and also in their assemblies. Such atomically precise NPs (or nanoclusters, NCs) bridge up with conventional NPs by providing unprecedented opportunities to reveal the specific patterns formed by intra- and inter-particle ligand interactions. In this Perspective, we first discuss how to achieve atomically precise NCs and determine their total structures. Then, we highlight the intra-particle ligand interactions (i.e., the ligand shell), including the various patterns formed on the NCs, the ligand patterning modes on facets and edges, and some aesthetic patterns assembled by ligands that are akin to biomolecular organization. The inter-particle ligand interactions and their roles in directing the self-assembly of NCs into coherent superlattices are also discussed, which provides a deep understanding of assembly mechanisms, with the insights from atomically precise NCs hinting for the assembly of conventional NPs. Overall, the success in achieving atomically precise NCs is expected to bring new opportunities to fields beyond nanochemistry, especially to materials design, engineering, and applications.

1. INTRODUCTION

Nanoscience has advanced significantly over the past two decades owing to the great successes in solution phase syntheses.[1−5] In early research, the polydispersity of nanoparticles (NPs) was a major issue, which motivated nanochemists to develop new synthetic methods to obtain monodisperse NPs (e.g., size distribution <10%), and nowadays many successful methods are available that allow excellent control over size and shape.[1−5]

In the solution phase, nanoparticles are typically protected by ligands or other stabilizers. With respect to the characterization, transmission electron microscopy (TEM) has become an indispensable tool. With TEM, the precise size and shape of NPs can be determined, and the chemical composition, crystalline structure, and valence state can also be analyzed. However, a fundamental limitation of TEM is that it is very difficult to see the ligands on the particle surface due to insufficient image contrast (Scheme 1a). Thus, understanding the details of ligands (such as the identity of ligands, their arrangement, and dynamic information) on NPs poses a major challenge in characterization of NPs. On the other hand, scanning tunneling microscopy (STM) has been utilized to image the ligand shells on NPs,[6,7] and there are also spectroscopic methods for probing the surface ligands,[6,8] as well as simulations,[9] but atomic resolution has not been achieved in real-space imaging.

The ligand issue also exists in nanoparticle assemblies (Scheme 1b). While monodisperse NPs can readily assemble into ordered superstructures via various interactions between NPs, the atomic and molecular level details of assembly remain

Scheme 1. Invisible Ligands (a) on the Nanoparticle Surface and (b) in the Assembly of Nanoparticles: Left, Schematic Diagrams, and Right, TEM Images of ∼5 nm NPs

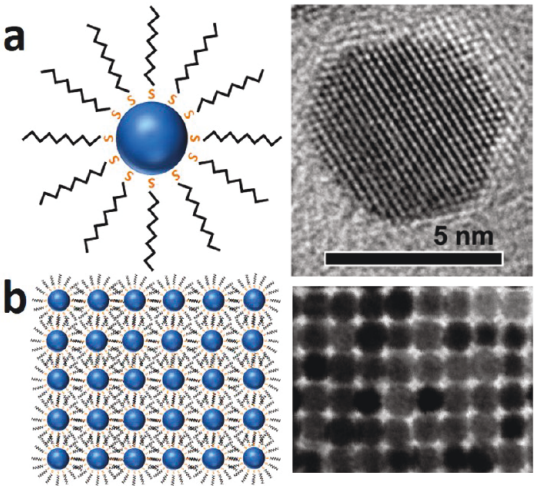

Received: May 29, 2020
Published: July 14, 2020

https://dx.doi.org/10.1021/jacs.0c05866
J. Am. Chem. Soc. 2020, 142, 13627−13644

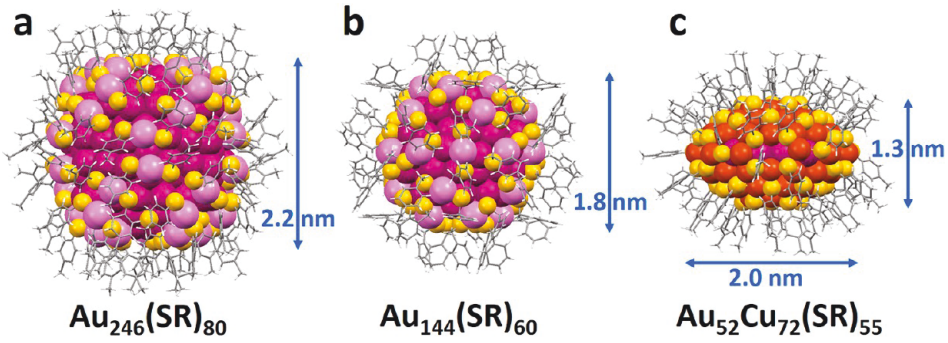

Figure 1. Total structures of (a) $Au_{246}(SR)_{80}$, (b) $Au_{144}(SR)_{60}$, and (c) $Au_{52}Cu_{72}(SR)_{55}$. Color labels: magenta/pink = Au, orange = Cu, yellow = S, gray = C, white = H. Redrawn from refs 41−43.

unclear.[10−16] When the inter-NP separations are smaller than 5 Å, exchange interactions may occur and lead to semiconducting, metallic, or even superconducting properties of the superlattice, depending on the NP composition.[17] The superlattices (or artificial solids) are appealing due to their new collective properties resulting from interactions between excitons, magnetic moments, or plasmons of NP building blocks, which can be utilized to fabricate functional devices.[13] Surface ligands are believed to kinetically influence the interactions between NPs and consequently their assembly. For example, by attaching single-stranded DNA to Au NPs, nanotubes of 3D architectures can form through self-association or other interactions of DNA structures.[18] Hairy polymers can tailor the interactions between Au NPs, directing the assembly into hybrid nanocomposites with customized architectures and collective properties.[19] From these perspectives, it is essential to understand and be able to control the behavior of surface ligands during the assembly.

To precisely map out the surface ligands on nanoparticles and understand the atomic/molecular level mechanisms, it is of paramount importance to determine the total structure of NPs. This calls for atomically precise NPs (also called nanoclusters, NCs). Progress in nanochemistry has led to the attainment of atomically precise metal NCs.[20−23] Their total structures and assemblies have been determined by single-crystal X-ray diffraction (SCXRD), which provides unprecedented opportunities for studying the ligand issues. In addition to the structures obtained,[20−28] ligand shells with unique patterns are observed on NCs, and such NCs are further used as precise building blocks to form hierarchical structures. Thus, NPs of atomic precision are very promising in bottom-up construction of functional materials with distinct properties. For example, the ordered surface pattern of ligands can facilitate specific interactions between reactants and catalysts by utilizing the ligands to induce a particular conformation for catalytic activity or selectivity control.[29,30] It is also clear that the chirality of NCs mainly originates from the chiral interface structure dictated by metal−ligand bonding.[31,32] A library of cluster-assembled solids has been designed,[33−36] in which the clusters (e.g., metal-chalcogenide ones) are held together via van der Waals interactions and/or inter-particle charge transfer (electrostatic forces), exhibiting tunable electrical transport, crystalline thermal conductivity, magnetic ordering, etc.[37] Self-assembly of atomically precise NCs has recently been reviewed,[37−40] but the significant roles of surface ligands have not been stressed yet.

In this Perspective, we focus on some salient features in the exquisite patterns formed by (1) the intra-NC ligand arrangements on the surface of metal NCs and (2) the NC assemblies in the macroscopic crystals directed by the inter-NC ligand interactions. We first illustrate the intra-NC ligand interactions that form various patterns in the ligand shells, and then the inter-NC ligand interactions that direct the self-assembly of NCs into coherent superlattices. We also relate the atomically precise NPs to conventional ones to emphasize the advantage of SCXRD for revealing the conformations and arrangements of ligands on the surface of the metal core and the interactions between NCs in the crystal lattices. The direct observation of ligands at atomic resolution (<1 Å) not only reveals the mysterious surface of NCs but also provides unprecedented details about the ligand shells and superlattices, which are critical in understanding the basic science of NCs and ensembles for applications.

2. HOW TO SEE LIGANDS ON NANOPARTICLES BY X-RAY DIFFRACTION?

X-ray crystallography has long been used in molecular chemistry to determine the structure of organic molecules and organometallic compounds. This technique has also been utilized in protein structure determination. When applying SCXRD to nanoparticles, the challenges are how to obtain atomically precise NPs and how to obtain single crystals of high quality.[20] While monodisperse NPs (though not atomically precise) readily form superlattices, no atomic-level structure of the surface and ligand interactions can be obtained by XRD because of the lack of long-range coherence in the superlattices. With atomically precise NPs, i.e., the NPs are all identical to each other at the atomic level, single crystals of the NPs can be obtained, and the ligands together with the inorganic core can be atomically resolved by SCXRD analysis.

Undoubtedly SCXRD is so far the most effective way to reveal the total structures of NPs; i.e., every atom (except H) can be identified and located with high accuracy, provided that high-quality crystals are grown from atomically precise NPs. Figure 1 shows examples of Au-thiolate (SR) and Au/Cu-thiolate NCs of atomic precision;[41−43] the completeness of the structures answers many scientific questions previously left unsolved for NPs. In addition, the details of ligand assembly on the surface of metal NPs can be explicitly seen, and aesthetic patterns have been unveiled. These specific patterns provide important information for inferring the surface structures of conventional NPs and their related properties.

https://dx.doi.org/10.1021/jacs.0c05866
J. Am. Chem. Soc. 2020, 142, 13627−13644

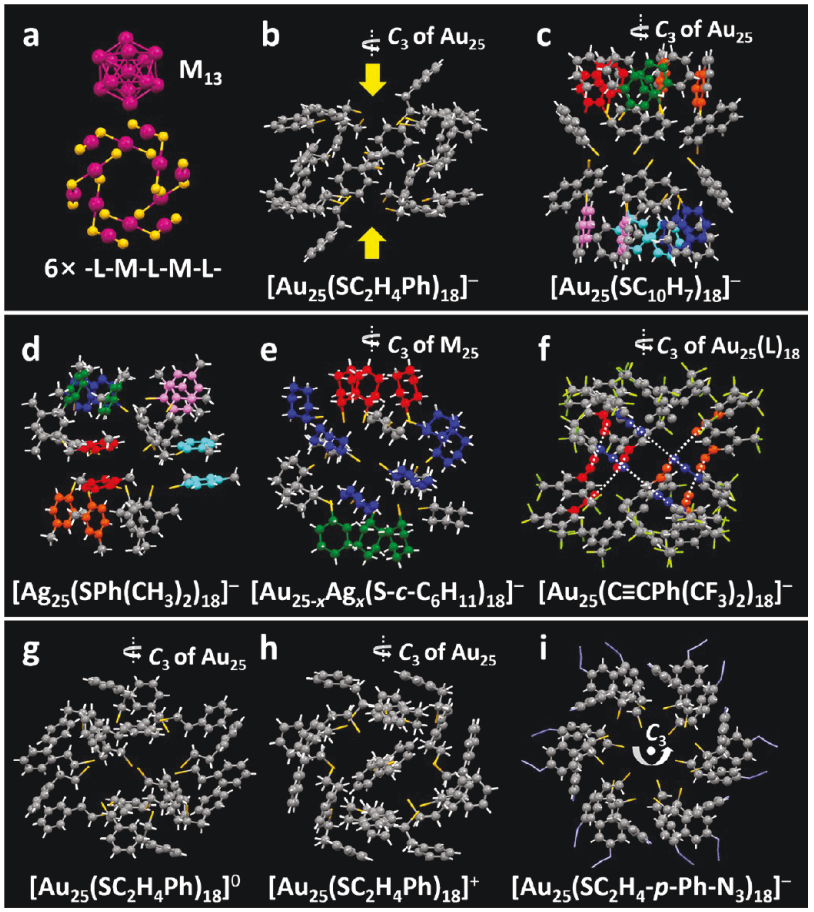

Figure 2. (a) Structure of the $M_{25}L_{18}$ core (M = Au/Ag). Different patterns formed by ligands on the surface of $[M_{25}(L)_{18}]^-$ NCs for (b) $[Au_{25}(SC_2H_4Ph)_{18}]^-$; (c) $[Au_{25}(SC_{10}H_7)_{18}]^-$; (d) $[Ag_{25}(SPh(CH_3)_2)_{18}]^-$; (e) $[(AuAg)_{25}(S\text{-}c\text{-}C_6H_{11})_{18}]^-$; (f) $[Au_{25}(SC{\equiv}CPh(CF_3)_2)_{18}]^-$; (g) $[Au_{25}(SC_2H_4Ph)_{18}]^0$; (h) $[Au_{25}(SC_2H_4Ph)_{18}]^+$; and (i) $[Au_{25}(SC_2H_4\text{-}p\text{-}Ph\text{-}N_3)_{18}]^-$. Color labels: magenta = Au, yellow = S, white = H, light green = F, other colors = C. Redrawn from refs 44−48, 55−57.

3. LIGAND ASSEMBLY ON THE SURFACE OF NANOCLUSTERS

Capping the NPs with ligands such as thiol, phosphine, amine, or other molecules stabilizes NPs. In addition, the ligand shell may also exhibit beautiful stripe and ripple patterns.[6] In this section, we focus on atomically precise NCs and illustrate the beautiful patterns formed on NCs with atomic resolution.

3.1. Ligand Assembly on M_{25} Nanoclusters. The 25-gold-atom NC (0.98 nm core, Au atomic center-to-center distance) formulated as $[M_{25}L_{18}]^-$ (M = Au/Ag, L = thiolate/alkynyl) is among the most well studied systems. The inner core is a 13-atom icosahedron and remains the same in various $[M_{25}L_{18}]^-$ NCs with different types of ligands.[44−48] The remaining 12 atoms of gold go to the surface and form six dimeric staple-like motifs, -L-Au-L-Au-L- (Figure 2a). Distinctively, the patterns formed by ligand organization can be dramatically different, albeit the M_{25} core is the same. In the structure of $[Au_{25}(SC_2H_4Ph)_{18}]^-$ (Figure 2b),[44] the ligands are less crowded on the surface along the C_3 axis, giving rise to two "pocket-like" cavities (Figure 2b, indicated by yellow arrows) exposing the Au atoms inside. These "pockets" were identified to be the active sites for electrochemical reduction of CO_2.[49]

By contrast, although the $[Au_{25}(SC_7H_{10})_{18}]^-$ (SC_7H_{10} = 1-naphthalenethoilates) NC has the identical $Au_{25}S_{18}$ core as that of $[Au_{25}(SC_2H_4Ph)_{18}]^-$, its ligand shell demonstrates significant non-covalent interactions between the 1-naphthalene groups,[45] showing $\pi\cdots\pi$ stacking (distances of 3.48−3.70 Å) (Figure 2c, marked in colored pairs). The total six pairs of $\pi\cdots\pi$ stacking are found to be around the quasi-C_3 axis of the Au_{25} core, covering the two "pockets" at the top and bottom. Density function theory (DFT) calculations find that aliphatic thiolates impart generally higher electrochemical and thermodynamic stability than aromatic thiolates for the structure of Au_{25};[50] however, experimentally, the thermal stability and anti-oxidation properties of $[Au_{25}(SC_{10}H_7)_{18}]^-$ are, instead, higher than those of Au_{25},[45] and there are also some interesting differences in catalysis when comparing non-aromatic and aromatic thiolate-protected Au_{25}.[30,45] The different patterns of ligand organizations caused by the inter-ligand interactions on the surface of $[Au_{25}(SR)_{18}]^-$ play a critical role in affecting the above properties.

$[Ag_{25}(SR)_{18}]^-$ (SR = 2,4-dimethylbenzenethiolate, SPh-$(CH_3)_2$) is the only silver counterpart reported so far to share the same structure as that of the Au_{25}, and the stabilizer needs to be an aromatic thiolate. The crystal structure of $[Ag_{25}(SR)_{18}]^-$ also reveals six pairs of $\pi\cdots\pi$ stacking (3.49−3.68 Å) between phenyl rings from adjacent thiolates (Figure 2d).[46] It is also observed that the thiolate pairs in the ligand shell of Ag_{25} are different from those of Au_{25} (Figure 2, panel c vs d), probably due to the distorted surface structure of Ag_{25}. The altered ligand orientation might be caused by minimizing

https://dx.doi.org/10.1021/jacs.0c05866
J. Am. Chem. Soc. 2020, 142, 13627−13644

Scheme 2. Atomically Precise Au-SR NCs with Different Types (Phases) of Core Structures[a]

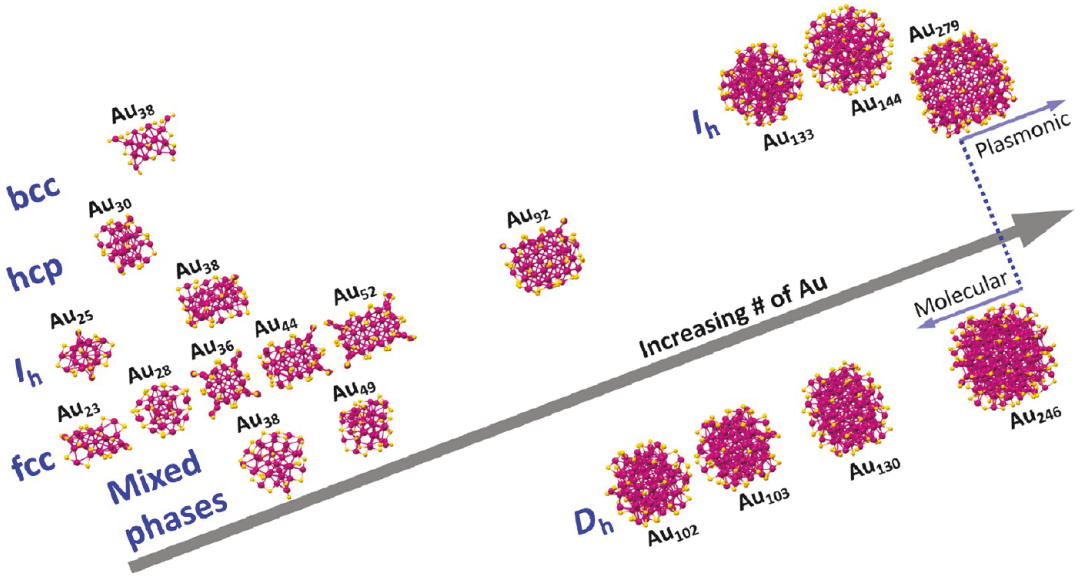

[a]Redrawn from refs 20 and 69.

the steric repulsion between adjacent ligands, especially when the phenyl rings have bulky methyl groups on them.

Upon heteroatom (Au or Ag) doping, the ligand shells of M_{25} NCs do not show detectable changes compared to their homo-gold or homo-silver counterparts as long as the ligands are the same, and Au-based M_{25} alloy NCs, i.e., $[Au_{25-x}Ag_x(SR)_{18}]^-$ (x up to 11), favor non-aromatic ligands,[51−53] whereas Ag-based M_{25} NCs, i.e., $[Ag_{25-x}Au_x(SR)_{18}]^-$ (x up to 8), prefer aromatic ligands,[54] which is consistent with the corresponding parent NCs. Moreover, the heavily Ag-doped M_{25} protected by cyclohexanethiolate, i.e., $[Au_{25-x}Ag_x(SR)_{18}]^-$ (SR = S-*c*-C_6H_{11}, $x \approx 20$),[55] exhibits another ligand pattern, in which the ligands are divided into different groups: three thiolates at the top and another three at the bottom (Figure 2e, marked in red/green), with the remaining 12 thiolates forming two chair-shaped bands around the waist of the NC (Figure 2e, marked in blue/gray). The average H···H distance between the ligands within the chair-shaped band is 2.54 Å, and that between the ligands in the top and bottom triangles is even shorter (avg. 2.40 Å), but there is no such interaction between the groups.

In addition to the different patterns caused by the different interactions between thiolate ligands, the recently solved alkynyl-protected $[Au_{25}(C{\equiv}CPh(CF_3)_2)_{18}]^-$ demonstrates a structure rearrangement of the six -L-Au-L-Au-L- motifs on the icosahedral Au_{13} kernel.[47] The different ligand shells (Figure 2, panels f vs b and c) stress the role of coordination between ligands and metal. In the V-shaped motif composed of three alkynyl groups and two staple Au atoms, the angle between terminal -C≡C- and Au is nearly linear, and two of such linear structures are parallel to each other (Figure 2f, marked in colored pairs with dashed lines). Due to the more stretched structure of the alkynyl ligands along the surface, i.e., the alkynyl ligands cover more surface area, it turns out that unreasonable contacts between phenyl groups would occur if the alkynyl-protected Au_{25} still adopts the same ligand pattern of thiolate-protected Au_{25};[47] thus, a structure rearrangement is instead adopted by alkynyl ligands on Au_{25}.

The charge state also has an impact on the surface ligand assembly. When oxidizing $[Au_{25}(SC_2H_4Ph)_{18}]^-$ to neutral (without changing the ligand),[56] the ligand shell transforms accordingly (Figure 2g), mainly due to the absence of the large counterion (tetraoctylammonium, TOA^+) which resides close to $[Au_{25}(SR)_{18}]^-$ in the crystal state due to electrostatic interaction, as well as the essential coplanarity of S-Au-S-Au-S motifs with the σ_h plane of the icosahedral core. Further removing one electron results in 6-electron $[Au_{25}(SC_2H_4Ph)_{18}]^+$, with another structure of the ligand shell (Figure 2h).[57] As the counterion (PF_6^-) is too small to have a major effect in the variation, it is likely that the distortion of the core in $[Au_{25}(SR)_{18}]^+$ caused by Jahn−Teller effect extends to the surface, resulting in different ligand orientations.

With the identification of every ligand in the ligand shell, it is possible to precisely functionalize the surface of Au_{25} NCs by site-specific ligand exchange.[58] Recently, a clickable azide-functionalized $[Au_{25}(SR)_{18}]^-$ was reported (Figure 2i),[48] in which the N_α's of the azide moieties ligated on the phenyl rings make an average C−C−N_α angle of ∼122.7°, indicating the primarily sp^2 character of the N_α, and the N_α−N_β−N_γ is almost linear, as indicated by SCXRD. Such a configuration enables the full amenability of azide moieties to strain-promoted alkyne−azide cycloaddition chemistry.[48]

Taken together, different patterns of ligands can be formed on the surface of the same $[M_{25}L_{18}]^-$ NC when one changes the ligands that stabilize the NC, and we expect that more patterns with distinct features will be obtained in future work when new ligands are explored. This is significant when considering that all these M_{25} NCs have an almost identical metal core. Such patterns are much richer compared to the thiolate monolayers formed on planar surfaces.[59]

3.2. Ligand Assembly on Facets and Edges of NCs.

The relatively small sizes of NCs exhibit diverse core structures, including the icosahedron and truncated decahedron, but the face-centered-cubic (fcc) core exposing well-defined Au{100} and Au{111} facets was not discovered until 2012.[60−63] Despite the relatively small facets of these fcc

https://dx.doi.org/10.1021/jacs.0c05866
J. Am. Chem. Soc. 2020, 142, 13627−13644

structures,[60−63] insightful information, including the ligand assembly on these facets, can still be derived. For comparison, Scheme 2 shows some selected Au-SR NCs with icosahedral (I_h),[42,44,64,65] fcc,[60−63,66−69] decahedral (D_h),[41,70−72] body-centered cubic (bcc),[73] hexagonal close-packed (hcp),[74] and mixed-phase structures.[25,75]

Parallel arrangement of thiolates is observed on the Au(100) facets of a series of Au NCs with fcc kernels.[62] For example, $Au_{92}(SR)_{44}$ and $Au_{52}(SR)_{32}$ (SR = 4-*tert*-butylbenzenethiolate, TBBT) have tetragonal structures with six flat and extended {100} facets (Figure 3a,b).[63,68] On these facets, each thiolate simply bridges two adjacent surface gold atoms, and all S atoms align in an orderly fashion, with the carbon tails having a nearly parallel alignment, tilting toward the facets in an ordered manner (Figure 3a,b, marked by different colors for different sets). Specifically, for both Au_{92} and Au_{52} NCs, the ligands on Au(100) facets are tilted toward the same direction in sets, whereas the ligands on Au(001) facets show opposite tilting directions (Figure 3a,b top vs bottom).

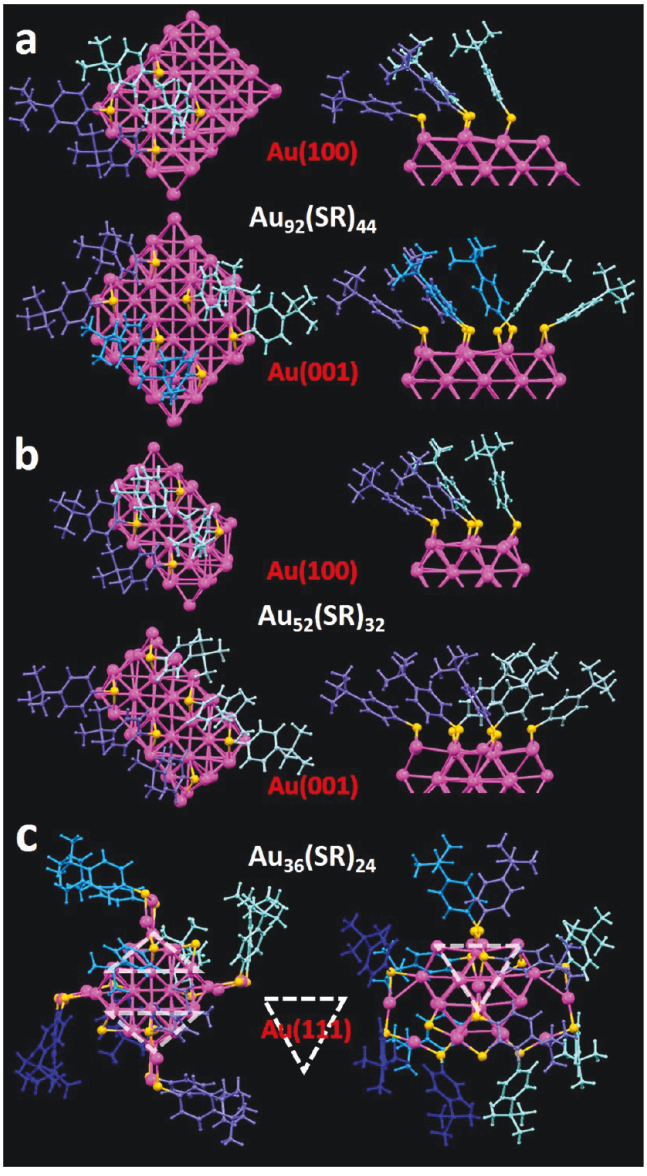

Figure 3. Top/side views of the ligand assembly on (a) the (100) and (001) facets of $Au_{92}(SR)_{44}$; (b) the (100) and (001) facets of $Au_{52}(SR)_{32}$; and (c) the (111) facets of $Au_{36}(SR)_{24}$. Color labels: magenta = Au, yellow = S, different blue = C/H. Redrawn from refs 60, 63, and 68.

Moreover, as to $Au_{92}(SR)_{44}$ with the largest Au{100} so far, the bridging thiolates at the edge sites of the facets show larger ∠S−Au{100} angles (~90°), resulting in tilting down of carbon tails to fill the extra volume at the edges; in contrast, the thiolates at the center of the surface have smaller ∠S−Au{100} angles (~70°) with carbon tails extending upward to avoid the surface tension (Figure 3a). The ligand overlayer has ~50% coverage, with one thiolate covering two Au atoms at the bridging sites on {100} facets of $Au_{92}(SR)_{44}$, in contrast to the low coverage of benzenethiolate and alkylthiolate monolayers on Au(111) facets, which are calculated to be 0.31 and 0.33, respectively.[76,77] These observations highlight the different features in thiolate assembly on atomically precise NCs of small size (1−3 nm in diameter) compared to the thiolate monolayers on bulk Au and conventional Au NPs of much larger size (both being the fcc structure).

$Au_{36}(SR)_{24}$ (SR = TBBT) is the first reported atomically precise NC to have a fcc kernel, and each of the four Au(111) facets is capped with one $Au_2(SR)_3$ staple motif.[60] When observing the ligand assembly on Au(111) in detail, it is found that the ligands are tilted toward the metal surfaces, resulting in a "windmill" arrangement to protect the tetrahedral kernel as much as possible to compensate the lower coverage of thiolates (Figure 3c). Due to the edge effect of the Au{100} and Au{111} facets in atomically precise NCs, versatile patterns from parallel, to tilting, to rotational ones have been demonstrated, which cannot be directly seen in conventional NPs. In future work, total structures of NCs with more extended Au(111) should be pursued, as the 6-atom Au(111) in the $Au_{36}(SR)_{24}$ is still not large enough to observe the "facet" effect.

3.3. Ligand Assembly into Rotational and Parallel Patterns. The rotational pattern in ligand assemblies on the surface of atomically precise NCs is best presented in the total structure of $Au_{246}(SR)_{80}$ (SR = *p*-methylbenzenethiolate, *p*-MBT, Figure 4a).[41] The protecting thiolates organize into rotational and parallel patterns, demonstrating a hierarchical structural complexity akin to biomolecule organization. Specifically, at the pole sites of the spherical core, 25 thiolates are rotationally arranged into four pentagonal circles (Figure 4b, left), and each circle has the same "latitude" and rotational direction, while at the waist, six thiolates are aligned into three alternating parallel pairs on each facet, and a total of 15 pairs reside around the pentagonal waist (Figure 4b, right). The ligand shell of $Au_{246}(p\text{-MBT})_{80}$ is stabilized by intra-NC C−H···π interactions; i.e., the C−H groups from the phenyl rings or the methyl groups interact with the π electrons of neighboring phenyl rings (Figure 4c, yellow dashed lines), with H···π distances in the range of 2.5−3.0 Å and C−H···π angle 112°−147°.[41] It should be noted that such interactions are found not only between the ligands at the same "latitude" but also between ligands from different "latitudes", thus giving rise to a 5-fold "swirl" pattern extending from the pole site to the waist of the NC (Figure 4c).

The C−H···π interaction is ubiquitous; for example, the crystal packing of complexes earlier demonstrated C−H···π interactions.[78] Now, in ligand-protected NCs, C−H···π is also observed.[41] In other atomically precise NCs, C−H···π interactions with avg. 2.80 Å distance are observed at the pole sites of $Au_{144}(SCH_2Ph)_{60}$ (Figure 5a,b, red dashed lines).

https://dx.doi.org/10.1021/jacs.0c05866
J. Am. Chem. Soc. 2020, 142, 13627−13644

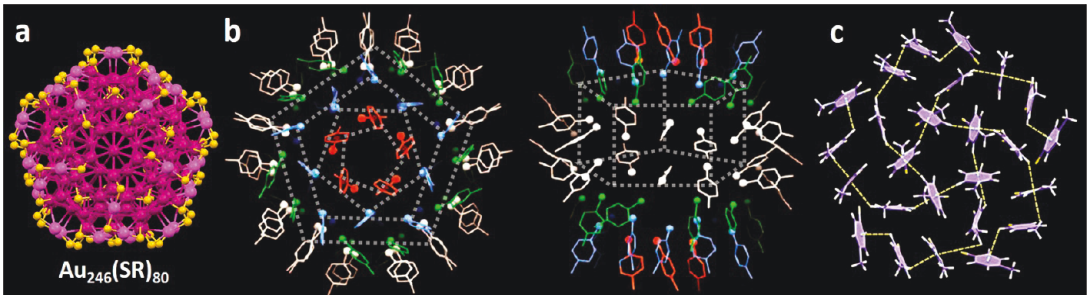

Figure 4. (a) The Au−S core of 2.2 nm $Au_{246}(SR)_{80}$. (b) The rotational pattern of ligands (red/blue/green) at the pole sites, and the parallel pattern of ligands (white) at the waist of $Au_{246}(SR)_{80}$; ligands at different "latitudes" are marked in different colors. (c) The C−H···π interactions in rotational patterns. Color labels: in the Au−S core, magenta/pink = Au, yellow = S. Panel a is redrawn from ref 41. Panels b and c are reproduced with permission from ref 41. Copyright 2016 American Association for the Advancement of Science.

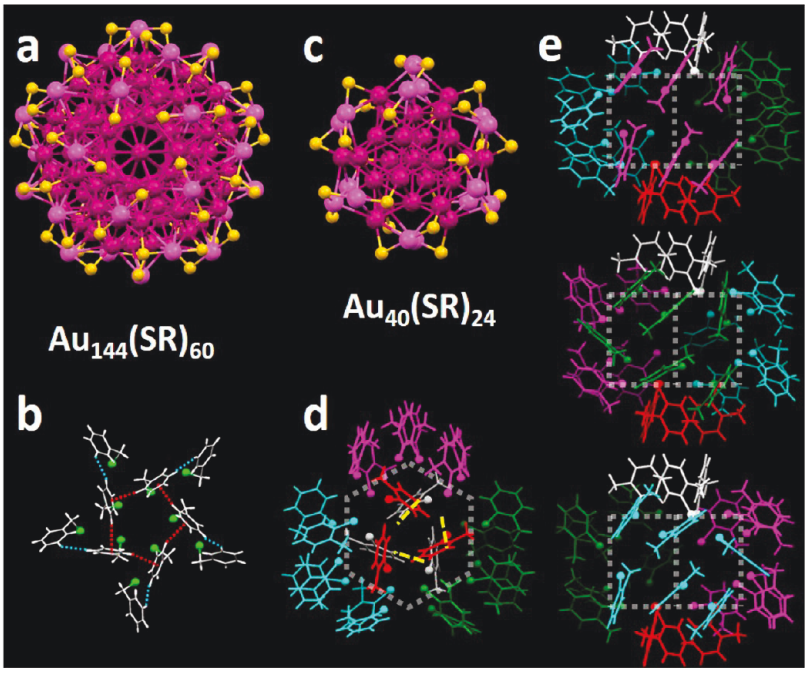

Figure 5. (a, b) The Au−S core and the rotational pattern within the ligand shell of $Au_{144}(SR)_{60}$ NC. (c) The Au−S core of $Au_{40}(SR)_{24}$. (d) The rotational pattern of ligands (red/white) at the pole sites via C−H···π interactions. (e) The parallel and perpendicular packing of ligands (magenta/green/cyan) at the waist of $Au_{40}(SR)_{24}$. Color labels: in the Au−S cores, magenta/pink = Au, yellow = S. Redrawn from refs 42 and 68.

Additional weak H···H interactions (avg. 2.73 Å) also form between the hydrogen atoms of two adjacent benzene rings in the same staple motif (Figure 5b, blue dashed lines),[42] enhancing the stability of the large NC. The 10 thiolates at each pole also demonstrate the spiral patterns in the assembly. We further illustrate the ligand shell on $Au_{40}(SR)_{24}$ (SR = *o*-methylbenzenethiolate, *o*-MBT), in which the gold kernel is a fcc hexagonal prism (Figure 5c).[68] The three thiolates on each Au(111) facet (top and bottom) spiral into a triangular pattern due to the C−H···π interactions (Figure 5d, yellow dashed lines); see section 3.3. As to the waist of the $Au_{40}(o\text{-MBT})_{24}$, the 18 thiolates can be divided into three groups (Figure 5e, magenta, green, and cyan). In the magenta group, thiolates are aligned in parallel (Figure 5e, top), whereas in the green and cyan groups (Figure 5e, middle/bottom), the thiolates in the middle are parallel, but the thiolates at the edges are aligned with different angles, or even perpendicular to the middle thiolates.

In the ligand shell of $Au_{102}(p\text{-MBA})_{44}$ (SR = *p*-mercaptobenzoic acid, *p*-MBA, Figure 6a), there are three types of ligand interactions (Figure 6b, left, from top to bottom): phenyl rings stack on one another; the phenyl rings form T-stacking; and the S atom interacts with the phenyl ring (avg. distance 3.55 ± 0.25 Å), resembling the aromatic-thiol π hydrogen bonding in proteins. Consequently, most of the thiolates are linked into multiple chains which extend from one pole of the NC to the other (Figure 6b, right).[70] As to the $Au_{133}(TBBT)_{55}$ NC, 24 -SR-Au-SR- staple motifs self-assemble on the spherical kernel from one pole and converge at the other, coiling up the extended curved surface of the NC with four highly ordered helices (Figure 6c). Moreover, it is found that, in the ligand shell, the carbon tails of the thiolates do not follow the helical stripe pattern of the staple motifs; rather, they self-organize into multiple "swirls" (Figure 6d, left), and each swirl is composed of four phenyl rings in a rotary arrangement (Figure 6d, right), resulting from the spherical core structure as well as the bulkiness of *tert*-butyl substituents which require a more compact packing mode.[65]

In all, ligand assembly on the surface of NCs can be clearly seen with the determined total structures of atomically precise

https://dx.doi.org/10.1021/jacs.0c05866
J. Am. Chem. Soc. 2020, 142, 13627−13644

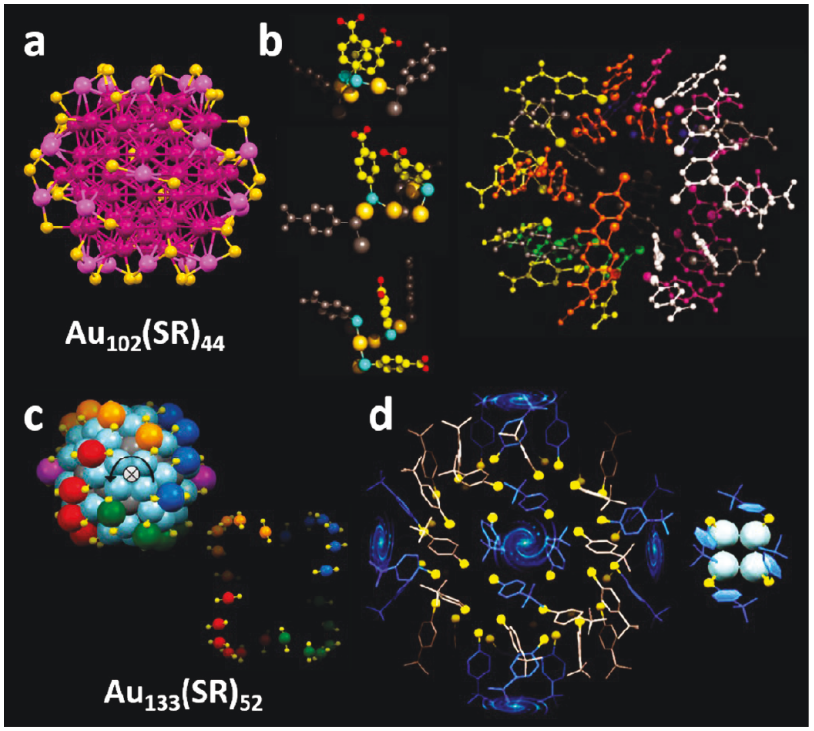

Figure 6. (a, b) The Au−S core and the ligand shell of $Au_{102}(p\text{-MBA})_{44}$. (c, d) The Au−S core and the ligand shell of $Au_{133}(TBBT)_{52}$. Color labels: in the Au−S cores, magenta/pink = Au, yellow = S. Panel a is redrawn from ref 70. Panel b is reproduced with permission from ref 70. Copyright 2007 American Association for the Advancement of Science. Panels c and d are reproduced with permission from ref 65. Copyright 2015 American Association for the Advancement of Science.

NCs. Rotational and parallel alignments of ligands and their interactions are evidenced. Some specific patterns and interactions are revealed, providing insights into the mysterious ligand shells that are critical in stabilizing NPs. Such insights also hint for the ligand shell structure in conventional NPs.[6]

3.4. Assembly of Bulky Ligands on NCs. With the solved structures of atomically precise metal NCs protected by bulky thiolates, e.g., adamantanethiolate (SAdm), it has been found that the assembly of single-component bulky ligands can also lead to ligand shells with specific patterns on the surface, which may be helpful for understanding the mixed-ligand patterns in conventional NPs.[6−9] The Zheng group reported a $[Ag_{141}(SAdm)_{40}X_{12}]^{3+}$ (X = Cl, Br, or I) NC of barrel shape (Figure 7a, top).[79] The Ag_{70} outer shell is mounted with 12 halogens as well as 40 thiolates around the C_5 axis at different latitudes, and the bulky SAdm ligands lead to a lower surface coverage (∼57%) for Ag_{141} NP compared to the ∼78% coverage for Ag_{136} NP capped by less bulky TBBT ligands, although the numbers of Ag atoms are comparable.[79,80] By a close check on the ligand shell of the Ag_{141} NC, we illustrate that the 40 SAdm ligands give rise to six circles (Figure 7a, marked in different colors) surrounding the metal core from one pole to the other, with the numbers of ligands in sequence of 5-5-10-10-5-5.

In 2004, Stellacci et al. used scanning tunneling microscopy to image ligand shells composed of a mixture of ligands, which showed parallel domains of ligand ripples encircling around the gold NPs.[81] One can now see in atomically precise NCs that even when NCs are protected by one type of thiolate, such patterns can also be formed. Of note, the "barrel-shaped" $Au_{130}(p\text{-MBT})_{50}$ NC[72] also has parallel ripples of ligands surrounding its core according to the distribution of sulfur atoms on the surface and NMR analysis on the surface ligands.

The ligand ripples can also be found on the surface of $Au_{30}(SAdm)_{18}$—which is very special due to its hcp core structure (Figure 7b, top).[74] As to its ligand shell, the total 18 thiolates form three parallel ripples from the top to the bottom around the Au_{30} core, with the top and bottom ripples being nearly triangular and the middle one hexagonal (Figure 7b, marked in different colors). It should be noted that the three-thiolate circles are arranged in a staggered conformation to avoid the repulsive collision between the bulky adamantane groups. Such a staggered alignment of neighboring circles is also found in the ligand assembly on the $[Ag_{141}(SAdm)_{40}X_{12}]^{3+}$ NC (Figure 7a). The macroscopic crystal of $Au_{30}(SR)_{18}$ NCs shows a fcc packing, which is the only example so far in gold NCs of atomic precision. The special "sandwich"-shaped ligand shell preserving the high symmetry of the NC's core should contribute to the unique packing and the nearly zero dipole moment of $Au_{30}(SAdm)_{18}$,[82] leading to anomalous solubility of this NC (only in benzene, not in other common solvents).

The parallel circle pattern of ligands is not the only conformation found in the ligand shells composed of bulky -SAdm. Li et al. recently reported a $Au_{19}Ag_4(SAdm)_{15}$ NC of *quasi*-C_3 symmetry, in which the arrangement of three $Au_3(SAdm)_4$ staple motifs imparts chirality to the NC (Figure 7c, top).[83] Interestingly, one can notice that the 15 adamantanethiolates constitute a triple-spiral along the C_3 axis (Figure 7c, marked in different colors), indicating that the ligand shell also contributes to the whole chirality of the NC. Very recently, Li et al. took a further step to manipulate the bimetallic NC into a trimetallic $Au_{19}Ag_3Cd_1(SAdm)_{15}Br$ NC by replacing the top $Ag(SAdm)_3$ motif with a novel $Cd(SAdm)_3Br$ motif, and the resulting NC shows a giant dipole moment ($\mu \approx 18$ D), mainly due to the introduced Cd−Br bond.[84] Note that the chiral pattern of the ligand shell, i.e.,

https://dx.doi.org/10.1021/jacs.0c05866
J. Am. Chem. Soc. 2020, 142, 13627−13644

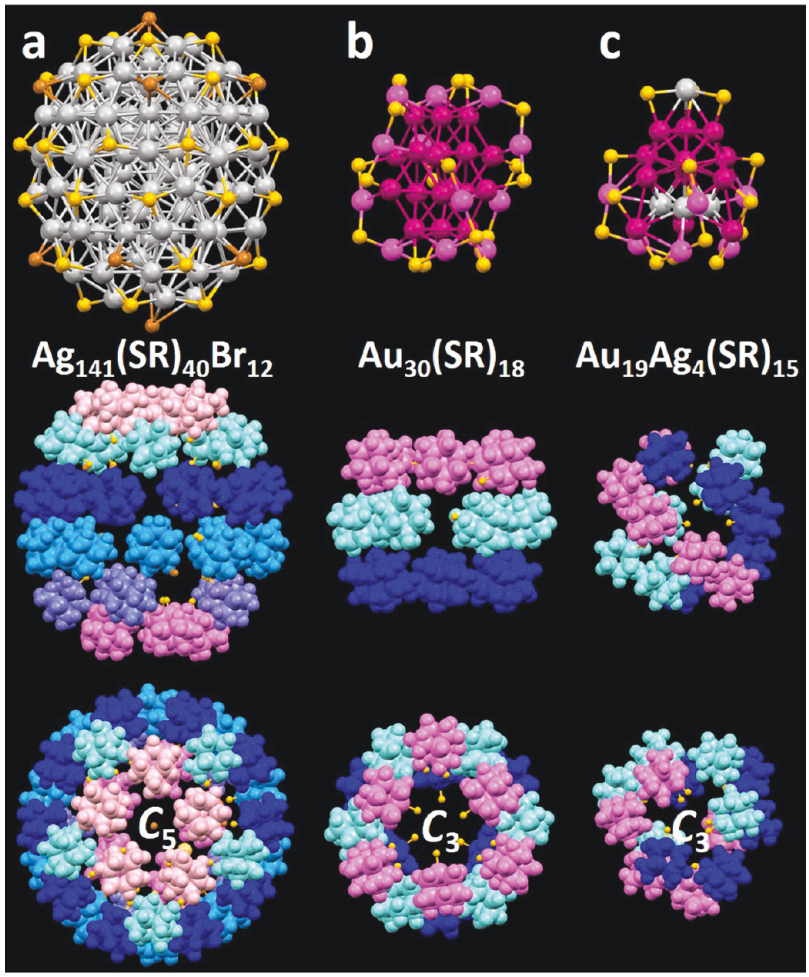

Figure 7. (a) The Ag−S−Br core and side/top views of the ligand shell of $Ag_{141}(SR)_{40}X_{12}$. (b) The Au−S core and side/top views of the ligand shell of $Au_{30}(SR)_{18}$. (c) The Au−S core and side/top views of the ligand shell of $Au_{19}Ag_4(SR)_{15}$. Color labels: in M−S cores, light gray = Ag, magenta/pink = Au, yellow = S, light brown = Br. Redrawn from refs 79 (panel a), 74 (panel b), and 83 (panel c).

the triple-spiral of ligands, also contributes to the total μ of the M_{23} (M = Au/Ag/Cd) NCs compared to other atomically precise $Au_n(SR)_m$ NCs with dipole moment being no more than 5 D.

4. INTER-PARTICLE ASSEMBLIES

The ordered superstructures of NPs are highly attractive to generate meso- and macro-scale materials with nanoscopic functionalities.[85,86] Self-assembly by controlling non-covalent interactions between NPs is a powerful tool to achieve structured systems at a molecular level.[87−89] Besides the commonly observed fcc and hcp packings, self-assembly into superstructures resembling quasicrystals,[15] chiral tetrahelices,[90] honeycombs,[91] clathrates,[92] etc. is quite appealing.

When the building blocks become atomically precise, the uniform composition and packing density in single crystals make the periodic assemblies especially attractive. Moreover, seeing the details of inter-NP ligand interactions is fulfilled, which provides unprecedented information for understanding the mystery of self-assembly at the atomic and molecular levels. Below we illustrate several examples.

4.1. Assembly Pattern of Large-Sized NCs of Atomic Precision. Ligand-protected atomically precise NCs composed of more than 100 metal atoms are quite informative in linking up with regular NPs. In section 3, we demonstrated the ligand assemblies on the surface of individual NC due to intra-NC ligand interactions, e.g., C−H···π interactions. In this section, we further discuss such interactions for directing the assembly of NCs into coherent superlattices.

Ligand interlocking in the lattice packing of $Au_{246}(p\text{-MBT})_{80}$ NCs (Figure 8a) leads to shorter inter-NP distance of 3.1 nm compared to the overall diameter of the NC (3.3 nm, the ligand shell included) and a monoclinic lattice with ∼60% packing density, deviating from the fcc lattice (density: 74%). The clockwise and counterclockwise rotational alignments of the surface ligands induce chirality in the NC[41] (see section 3.3). The NCs with the same chirality are stacked in the same square layer (Figure 8b, denoted *R*/*L*), and each $Au_{246}(p\text{-MBT})_{80}$ NC has six nearest neighbors, four of which have the same chirality as the central one. Figure 8c shows the ligands of four pentagonal $Au_{246}(p\text{-MBT})_{80}$ NCs: the central NC (colorful), two neighboring NCs of the same chirality (yellow), and one neighboring NC of opposite chirality (purple). The surrounding NCs interact with the central one via ligand alignment at the pole sites due to the higher packing density of these rotational ligands (∼14 nm^{-2}).[41] Besides, symmetry matching also significantly affects the ordered assembly. For the adjacent NCs with the same chirality as the central one, the pentagons are aligned in a side-by-side manner (Figure 8d, top), whereas for those with opposite chirality, the pentagons

https://dx.doi.org/10.1021/jacs.0c05866
J. Am. Chem. Soc. 2020, 142, 13627−13644

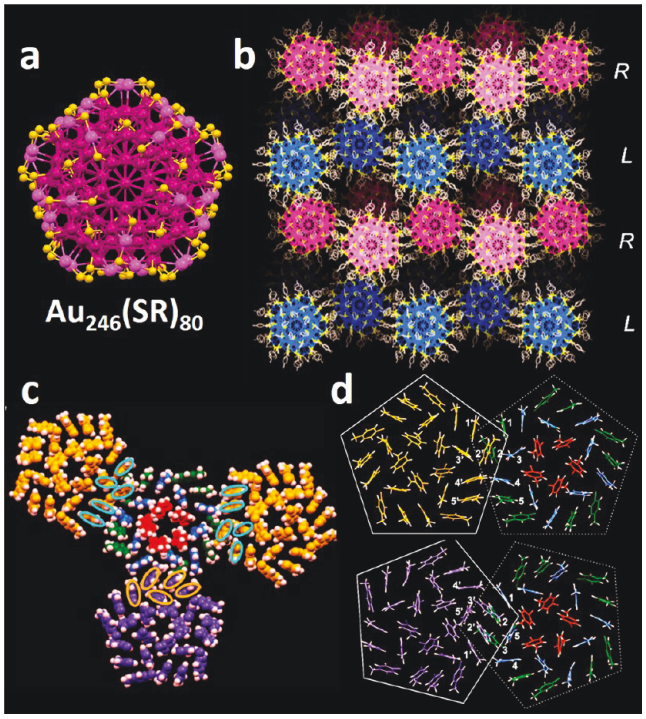

Figure 8. (a) The Au−S core of $Au_{246}(p\text{-MBT})_{80}$. (b) $Au_{246}(p\text{-MBT})_{80}$ NCs in the crystal lattice for (c) inter-NP ligand interactions, including side-by-side stacking of ligands from $Au_{246}(p\text{-MBT})_{80}$ NCs with the same chirality (d, top) and point-to-point stacking of ligands from $Au_{246}(p\text{-MBT})_{80}$ NCs with opposite chirality (d, bottom). Panel a is redrawn from ref 41. Panels b−d are reproduced with permission from ref 41. Copyright 2016 American Association for the Advancement of Science.

are aligned in a point-to-point manner (Figure 8d, bottom), with interacting ligands' spacing of 1.9−2.5 Å. The symmetry-matching strategy resembles the pattern of multiple engaged gears, with each contacting area akin to a tooth of the gear. Taking the thiolate itself as the primary structure, the C−H···π interactions among the ligands lead to more complex secondary surface patterns, and the density- and symmetry-dictated packing rules further guide the assembly of $Au_{246}(p\text{-MBT})_{80}$ NCs into the tertiary structure in the crystal lattice.[41]

The best example so far to demonstrate the inter-particle C−H···π interactions is found in the assembly of $Au_{103}S_2(SC_{10}H_7)_{41}$ (SC_7H_{10} = 2-naphthalenethiolate) NCs (Figure 9a). In addition to the π···π stacking in the ligand shell of single $Au_{103}S_2(SC_{10}H_7)_{41}$, patterns induced by intra- and inter-NC C−H···π interactions can also be clearly identified (Figure 9b).[71] Specifically, two naphthalene groups form a dimer via the edge-to-face T-shaped C−H···π interactions, in which one naphthalene perpendicularly stands on the other. The interactions between the T-shaped dimer on one NC and another dimer on the neighboring NC give rise to a tetramer, which is reminiscent of a "herringbone pattern" in the ligand interactions (Figure 9c). The average distance for the C−H···π interaction in the inter-NC tetramer is ∼2.58 Å, shorter than the intra-NC distance of ∼2.73 Å. The connectivity of ligands via the herringbone-like C−H···π interactions extends along the *z*-axis of the unit cell, resulting in a needle-like single-crystal superstructure along the [001] direction.[71]

It is worth noting that, although different bonding modes of Cu-SR from Au-SR lead to different surface structures on the NCs,[32] the intra- and inter-particle interactions between ligands are not affected by M−S coordination. A recent work on a pentagonal $Au_{52}Cu_{72}(p\text{-MBT})_{55}$ alloy NC (Figure 9d) demonstrated symmetry (D_{5h})-related assembly, and the aromatic thiolates mounted on the "3D Penrose tilling"-like cage of Cu-SR interact via C−H···π interactions (Figure 9e), resulting in a "quadruple-gear" interlocking pattern.[43] As to the long-range pattern in the crystal, the interlocking pattern repeats along the *x*-axis infinitely, forming one-dimensional

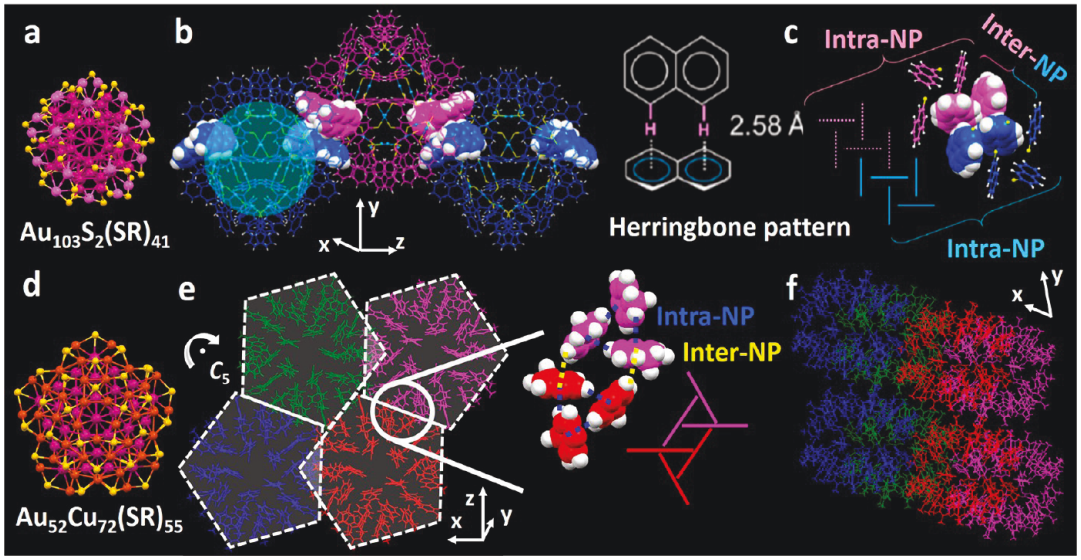

Figure 9. (a) The Au−S core of $Au_{103}S_2(SC_{10}H_7)_{41}$. (b) The intra-/inter-NC C−H···π interactions between ligands of $Au_{103}S_2(SC_{10}H_7)_{41}$ NCs in the crystal lattice. (c) Combination of intra-/inter-NC ligand−ligand interactions into a herringbone pattern. (d) The Au−S core of $Au_{52}Cu_{72}(p\text{-MBT})_{55}$. (e) The interacting ligands from the four nearest $Au_{52}Cu_{72}(p\text{-MBT})_{55}$ NCs with the C−H···π interactions highlighted. (f) Twin nanowires composed of interlocked $Cu_{72}Au_{52}(p\text{-MBT})_{55}$ NCs along the *x* axis. Color labels: in M−S cores, magenta/pink = Au, orange = Cu, yellow = S. Panel a is redrawn from ref 71. Panels b and c are reproduced with permission from ref 71. Copyright 2017 American Chemical Society. Panels d−f are redrawn from ref 43.

https://dx.doi.org/10.1021/jacs.0c05866
J. Am. Chem. Soc. 2020, 142, 13627−13644

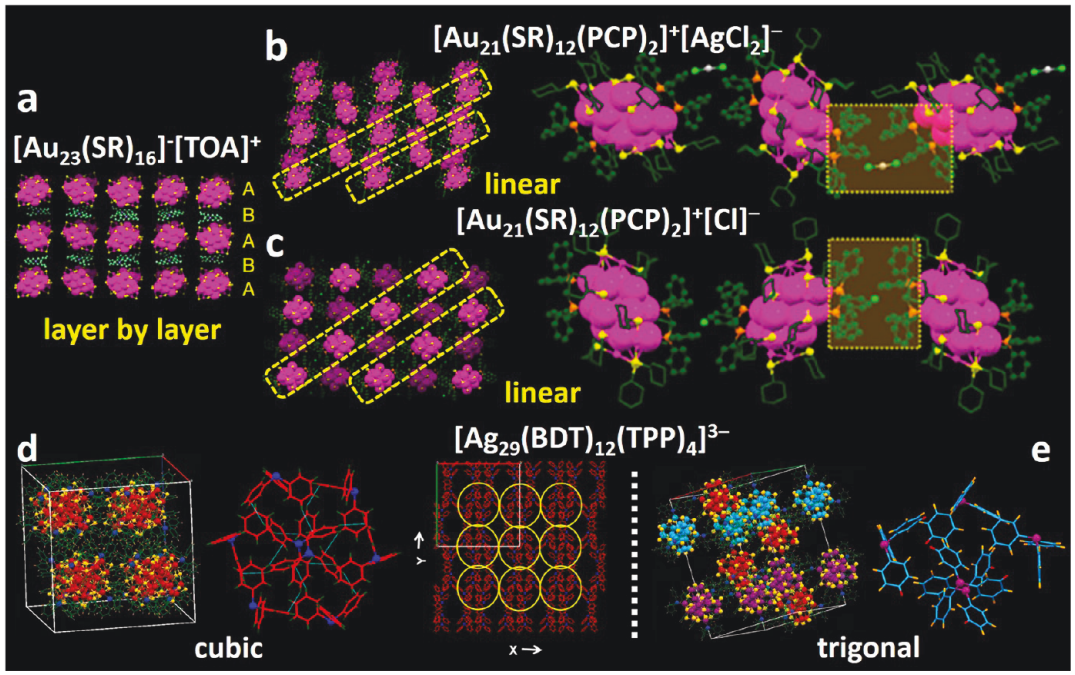

Figure 10. (a) Layer-by-layer packing of $[Au_{23}(SR)_{16}]^-[TOA]^+$ NCs in single crystals. (b) 3D linear packing (left) and 1D assembly (right) of $[Au_{21}(SR)_{12}(PCP)_2]^+[AgCl_2]^-$ NCs. (c) 3D linear packing (left) and 1D assembly (right) of $[Au_{21}(SR)_{12}(PCP)_2]^+[Cl]^-$ NCs; yellow areas highlight the surface hooks connecting two neighboring Au_{21}NCs. Color labels: magenta = Au, gray = Ag, light green = Cl, yellow = S, orange = P, green = C; H atoms are omitted for clarity. (d) Cubic unit cell of $[Ag_{29}(BDT)_{12}(PPh_3)_4]^{3-}$ NCs, the corresponding C−H···π interactions between the PPh_3 ligands in the ligand shell, and the packing of PPh_3 ligands in the crystal lattice. (e) Trigonal unit cell of $[Ag_{29}(BDT)_{12}(PPh_3)_4]^{3-}$ NCs and corresponding C−H···π interactions between the TPP ligands in the ligand shell. Panels a−c are reproduced with permission from ref 93. Copyright 2018 Springer Nature and distributed under the terms of the Creative Commons CC BY license. Panels d and e are reproduced with permission from ref 39. Copyright 2019 American Chemical Society.

twin nanowires composed of highly connected NCs, whereas along the *y*- or *z*-axis, the NCs belonging to different twin nanowires have no such interactions (Figure 9f).

4.2. Correlated NCs with Different Inter-NC Assemblies. In the research on NCs, the most valuable information comes from correlated NCs. In other words, maintaining as many features as possible while changing one variable can result in correlated NCs, which provides the most effective way to figure out the specific roles of the variable in the system. Such an ideal condition is usually presumed in the study of conventional NPs. In atomically precise NCs, however, strict preconditions can be easily fulfilled as every detail is definitive, making the comparison more straightforward and informative.

We first discuss an example in which the associated counterion can guide the hierarchical self-assembly of NCs in a delicate manner and consequently change the electrical transport properties of the solid states. Two Au_{21} NCs, i.e., $[Au_{21}(SR)_{12}(PCP)_2]^+[AgCl_2]^-$ and $[Au_{21}(SR)_{12}(PCP)_2]^+Cl^-$ (SR = S-*c*-C_6H_{11}, PCP = bis(diphenylphosphinomethane), which are derived from $[Au_{23}(SR)_{16}]^-[TOA]^+$, are used as building blocks in superstructure assembly.[93] Compared to the original $[Au_{23}(SR)_{16}]^-[TOA]^+$, in which the NCs pack into an orthorhombic lattice with $[Au_{23}(SR)_{16}]^-$ and $[TOA]^+$ in a layer-by-layer manner (Figure 10a), the Au_{21} NCs with respective counterions $AgCl_2^-$ and Cl^- linearly pack into triclinic (Figure 10b, left) and monoclinic (Figure 10c, left) lattices, respectively. The linear arrangement is driven by the inter-NC interactions of the "surface hooks" composed of four phenyl groups from two neighboring Au_{21} NCs (Figure 10b,c, right), and one $[AgCl_2]^-$ or $[Cl]^-$ counterion resides inside the phenyl cage, resulting in $\pi\cdots\pi$ pairs (5.0−5.8 Å) as well as C−H···Cl interactions (2.5−3.3 Å). The Au_{21} NCs can assemble into 1D nanofibrils via the $\pi\cdots\pi$ and C−H···Cl interactions, and further into 3D single crystals. Interestingly, the different associated counterions can significantly change the electrical transport properties of the NC-assembled solids by 2 orders of magnitude due to the altered configurations of the surface hooks.[93]

Based on atomically precise $[Ag_{29}(BDT)_{12}(PPh_3)_4]^{3-}$ (BDT = 1,3-benzenedithiol) building blocks, cubic and trigonal superlattices can be achieved via slow evaporation of dimethylformamide (DMF) solution and vapor diffusion of methanol into the DMF solution, respectively (Figure 10d,e),[94,95] resembling the polymorph previously reported in the superlattices of metal or semiconductor NPs.[96,97] It is evident from SCXRD that the C−H···π interactions between PPh_3 ligands are much stronger (~2.88 Å) in the cubic superlattice, resulting in polymeric chains in the crystal lattice (Figure 10d), whereas the C−H···π distances in the trigonal system are only ~3.12−3.37 Å (Figure 10e), too discontinuous to form ligand chains. Due to the higher rigidity facilitated by the C−H···π interactions, the single crystals with cubic lattice are more luminescent compared to their less emissive counterparts with trigonal lattice.[95]

Ligands are critical in directing the assembly of NPs into superlattices with controlled organization.[98] In the assemblies of neutral Au_{25} NCs protected by short-chain alkylthiolates, i.e., ethanethiolate (SC_2H_5) and *n*-butanethiolate (SC_4H_9), $[Au_{25}(SC_4H_9)_{18}]^0$ shows the formation of a linear polymeric chain linked by Au−Au bonds (~3.15 Å) between NCs.[99] The two closest staple motifs of neighboring $[Au_{25}(SC_4H_9)_{18}]^0$ NCs are oriented almost perpendicularly to each other, and the

https://dx.doi.org/10.1021/jacs.0c05866
J. Am. Chem. Soc. 2020, 142, 13627−13644

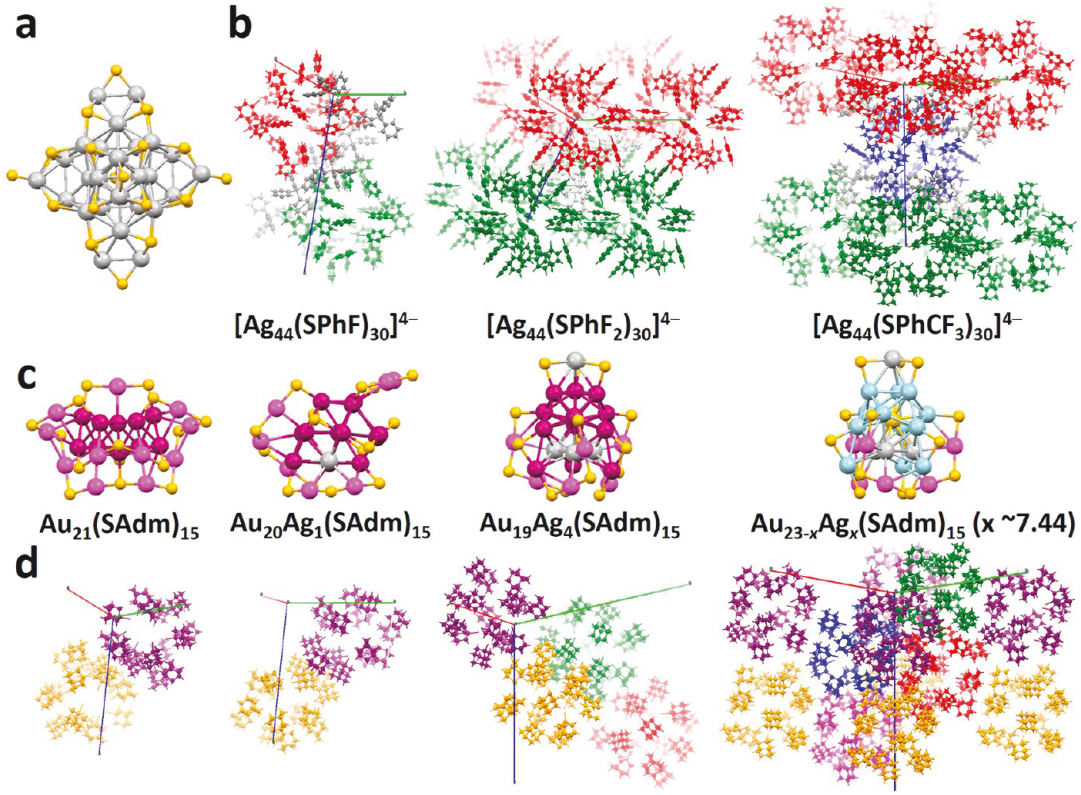

Figure 11. (a) The Ag−S core and (b) inter-NC assembly for $[Ag_{44}(SPhF)_{30}]^{4-}$, $[Ag_{44}(SPhF_2)_{30}]^{4-}$, and $[Ag_{44}(SPhCF_3)_{30}]^{4-}$ in crystal lattices, respectively. (c) The M−S (M = Au/Ag) cores and (d) corresponding inter-NC self-assembly for $Au_{21}(SAdm)_{15}$, $Au_{20}Ag_1(SAdm)_{15}$, $Au_{19}Ag_4(SAdm)_{15}$, and $Au_{23-x}Ag_x(SAdm)_{15}$ ($x \approx 7.44$) in crystal lattices. Color labels: in M−S cores, magenta/pink = Au, light gray = Ag, light blue = Au/Ag, yellow = S. Redrawn from refs 101 (panels a and b) and 83 (panels c and d).

alkyl groups on each staple are oriented in a up/down/up manner, resulting in aurophilic interactions. However, the assembly of "nearly naked" $[Au_{25}(SC_2H_5)_{18}]^0$ with even shorter capping thiolates does not show such a pattern; i.e., the average Au···Au distance of 4.12 Å is not close enough to form strong interactions.[100] A "twist-and-lock" mechanism was proposed, suggesting that the ∼90° twist allows the interdigitation of the butanethiolates, whereas too short (no lock) or too long (steric hindrance) ligands hamper sufficiently short inter-NC distances.[99]

Several types of $[Ag_{44}(SR)_{30}]^{4-}$ NCs (Figure 11a,b) protected by hydrophobic thiolates (SR = SPhF, $SPhF_2$, and $SPhCF_3$) were reported, and their space groups and the lattice constants of the unit cells can be varied when applying different fluorinated arylthiols (Figure 11b).[101] It should be noted that, in spite of the large differences in NC assemblies, the building blocks ($Ag_{44}S_{30}$, Figure 11a) are identical in all three superlattices, stressing the determinative role of ligands in directing the assembly. We propose that the following factors be responsible for the various patterns: (1) the fluoro substituent(s) on the phenyl rings, which might introduce intra- and inter-NC hydrogen bonding; (2) the steric effect due to different positions and bulkiness of the substituted groups; and (3) the volume and electrostatic influence of counterions (Figure 11b, gray molecules) inside the superlattices.

A series of correlated NCs by asymmetric doping of Ag into ligand-protected homogold NC has been reported, i.e., from $Au_{21}(SAdm)_{15}$ to $Au_{20}Ag_1(SAdm)_{15}$, then to $Au_{19}Ag_4(SAdm)_{15}$, and finally to $Au_{23-x}Ag_x(SAdm)_{15}$ ($x > 4$) NCs with increasing Ag ratio in the precursors (Figure 11c).[83] Size and structural evolutions are revealed by SCXRD; of note, the number and type of ligands remain the same, i.e., 15 adamantanethiolate for all the NCs in the series. With this series, an interesting relationship between the symmetry of M−S core and the symmetry of self-assembly is revealed after excluding the effects of other potential factors, including the counterion (i.e., no counterion for neutral NCs), the solvent (the same combination of solvent/anti-solvent in crystallization), and the ligand−ligand interactions (no $\pi\cdots\pi$ or C−H$\cdots\pi$ interactions) in this series. As the symmetry of the core improves, the packing of the superlattices becomes more symmetric, i.e., from triclinic to monoclinic, then to trigonal (Figure 11d).[83] One mystery lies in whether the symmetry of the ligand assembly on an individual NC decides the self-assembly of the NCs, or if the latter has any impact on the ligand orientations.

The above NC-to-crystal symmetry relationship can also be applied to other related NCs prepared by ligand exchange, for example, $Au_{28}(SR)_{20}$ (SR = TBBT or S-*c*-C_6H_{11}) and $Au_{36}(SR)_{24}$ (SR = TBBT or SPh), in which the NCs with cores of C_2 symmetry correspond to superlattices of relatively higher symmetry.[83] As to $Au_{38}(SR)_{24}$ (SR = SC_2H_4Ph or $SPh(CH_3)_2$), the non-aromatic ligand-protected NCs self-assemble into triclinic lattice, whereas the aromatic ligand-protected NCs with C_3 symmetry pack into trigonal superlattice. The total structure of the latter demonstrates intra-NC $\pi\cdots\pi$ stacking of the ligands as well as the "anagostic" C−H··· Au interactions inside the ligand shell.[102] However, no obvious inter-NC interaction between the ligands can be observed in all

https://dx.doi.org/10.1021/jacs.0c05866
J. Am. Chem. Soc. 2020, 142, 13627−13644

the above comparisons, indicating that the symmetry of the core might indicate the manner of inter-NC packing.

The Wu group successively reported two related NCs, i.e., $Au_{60}S_6(SR)_{36}$ and $Au_{60}S_7(SR)_{36}$ (SR = SCH_2Ph), with the only difference being a foreign sulfur atom inserted into the center of the Au_4 tetrahedron located at one corner of the $Au_{60}S_6$ core to obtain $Au_{60}S_7$; i.e., the introduced single S only leads to a local structure change (Figure 12a,b, top, S marked in

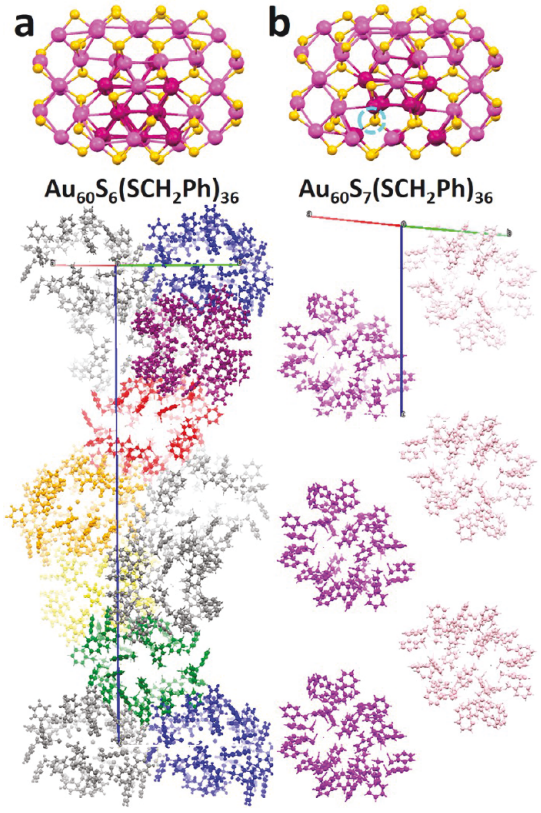

Figure 12. The Au−S cores and corresponding inter-NC self-assembly for (a) $Au_{60}S_6(SCH_2Ph)_{36}$ and (b) $Au_{60}S_7(SCH_2Ph)_{36}$. The left-handed helix in the lattice of $Au_{60}S_6(SCH_2Ph)_{36}$ NCs is highlighted in rainbow color. Color labels: in Au−S cores, magenta/pink = Au, yellow = S. Redrawn from refs 103 (panel a) and 104 (panel b).

circle).[103,104] However, a significant alternation is manifested in the packing patterns of the superlattices despite the same crystallization conditions. Specifically, $Au_{60}S_6$ NCs grow into the 6H left-handed helical arrangement (Figure 12a), while $Au_{60}S_7$ NCs adopt the "ABAB" organization (Figure 12b). It is clear from the comparison that $Au_{60}S_7$ NCs in the lattice are sparsely packed without any strong ligand−ligand interaction, while the packing of $Au_{60}S_6$ NCs is much denser. We deem that the C_2 axis in the $Au_{60}S_6$ NC makes it more symmetric, thus facilitating the formation of an ordered pattern in the lattice; by contrast, the insertion of an additional S certainly breaks the symmetry of the NC, resulting in simple alternation in the $Au_{60}S_7$ crystal.

The $Au_{30}(SAdm)_{18}$ NCs self-assemble into a fcc superlattice rarely observed in the case of atomically precise NCs,[74] although such a lattice is commonly observed in the assembly of conventional NPs.[98,105,106] The high symmetry of $Au_{30}(SAdm)_{18}$, having both a C_3 axis and an inversion center, might contribute to this special phenomenon. This rationale is consistent with the general observation in conventional NPs that spherical geometry usually leads to a fcc or hcp lattice, while anisotropic NPs, e.g., tetrahedral shape, are promising for achieving superlattices with extraordinary packing patterns.

4.3. Inter-NC Assemblies Mediated by Hydrogen Bonds. Experiment and theory have revealed the mechanism for the self-assembly of gold NPs via hydrogen bonds and electrostatic repulsions.[12,13,107−109] Calculations indicate that the most stable conformers for the protonated−deprotonated adducts of gold NPs capped by 4-mercaptophenol and protonated cysteine have nearly coplanar hydrogen bonds.[110]

Here we illustrate the atomic-resolution hydrogen-bonding network in a superlattice. The pattern and interactions inside the ligand shell of $Au_{102}(SR)_{44}$ (SR = *p*-MBA) NC have been discussed in section 3.3,[70] and the inter-NC H-bonds can also direct the self-assembly of the NCs into superstructures.[111] The combination of NMR, DFT, and molecular dynamics simulations indicates that the thiolates have an intrinsic orientation in water closely related to their arrangement in the solid state.[111] By controlling the protonation/deprotonation balance of the *p*-MBA ligands, template-free 2D nanosheets as well as closed spherical capsids can be obtained in solution, driven by the spontaneous patchiness (i.e., directions of H-bonds are not equally distributed over the NC) of the ligands on $Au_{102}(SR)_{44}$ NCs.[112]

Direct observation of hydrogen bonds in NCs assembly is achieved by water-dispersible Ag NCs of atomic precision, i.e., $[Ag_{44}(SR)_{30}]^{4-}$ (SR = *p*-MBA).[115,116] In the structure of $[Ag_{44}(SR)_{30}]^{4-}$, the icosahedral Ag_{12} (I_h-Ag_{12}) is encapsulated by a dodecahedral Ag_{20} (D_h-Ag_{20}) and further protected by six $Ag_2(SR)_5$ mount motifs in an octahedral manner (Figure 13a).[116] The triclinic unit cell of a $[Ag_{44}(SR)_{30}]^{4-}$ crystal contains two NCs (α/β) with mirror symmetry, with the α and β NCs occupying the neighboring layers (Figure 13b, where the α and β NCs are distinguished by marking the I_h-Ag_{12} in red and magenta, respectively).[117] The layers are staked into a lattice with A, B. and C layers (Figure 13b, A/B/C layers are distinguished by coloring the D_h-Ag_{20} in light green, dark green, and black, respectively), resulting in a 6-layer sequence of Aα, Bβ, Cα, Aβ, Bα, Cβ. Surprisingly, the *p*-MBA ligands bundle in two ways: the intra-layer L_2 binding between $\alpha-\alpha$ or $\beta-\beta$ Ag_{44} NCs involves interfacing doubly bundled ligands (Figure 13c, top), and the inter-layer L_3 binding between $\alpha-\beta$ Ag_{44} NCs involves interfacing triple-bundled ligands (Figure 13c, bottom). In the highly connective superlattice network, there are 60 H-bonds total (24 intralayer and 36 interlayer) formed between 30 pairs of *p*-MBA ligands relating one central Ag_{44} NC to its six nearest neighbors.

Various objects, including carbon nanotubes[118,119] and copolymers,[10] can be used as templates for metal NP organization. Strong interactions between the template and NPs lead to highly ordered superstructures that are predefined by the shape of the templates. The Pradeep group modified the surface of Te nanowires (NWs) with $[Ag_{44}(SR)_{30}]^{4-}$, resulting in a cross-bilayer structure in which the NWs in the same layer were parallel, with uniform inter-NW distances of ~3.4 nm for both layers and an angle of 81° between the two adjacent layers (Figure 13d,e). The Ag_{44} NCs attached on Te NWs via the COO^- groups of some ligands, leaving the other carboxyl groups free to form H-bonds when the Ag_{44}@Te NWs come closer. Thus, it is derived that the H-bonds might be the driving force for the highly ordered woven-fabric-like assemblies of the composites.[113] In another study, *p*-MBA-

https://dx.doi.org/10.1021/jacs.0c05866
J. Am. Chem. Soc. 2020, 142, 13627−13644

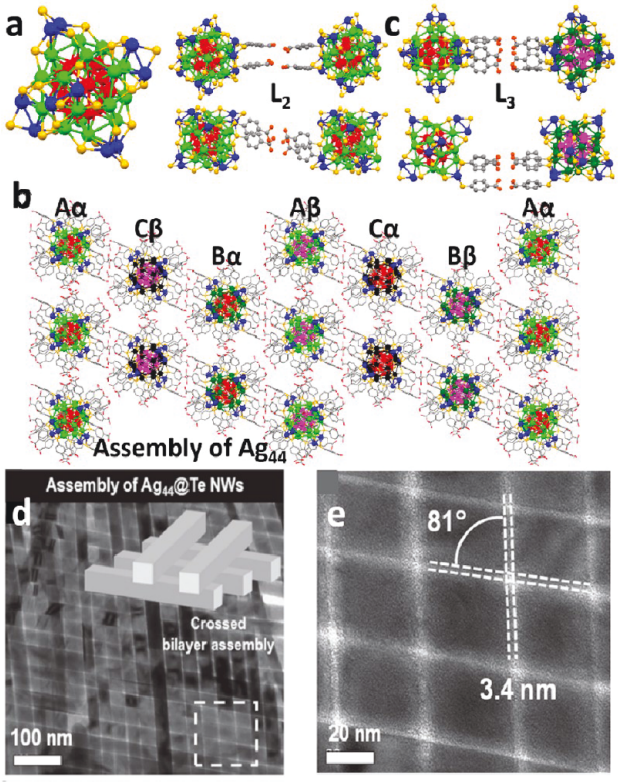

Figure 13. (a) The Ag−S core and (b) the fcc superlattice of $[Ag_{44}(p\text{-MBA})_{30}]^{4-}$ NCs. (c) Two views of the hydrogen bonds (L_2 and L_3) between two neighboring Ag_{44} NCs. (d) TEM image of the crossed-bilayer assembly of Ag_{44}@Te NWs; inset: schematic illustration of the crossed bilayer assembly. (e) Enlarged view of the marked region in (d). Panels a−c are redrawn from ref 116. Panels d and e are reproduced with permission from ref 113. Copyright 2016 Wiley-VCH Verlag GmbH & Co. KGaA, Weinheim.

functionalized gold nanorods (GNRs) were mixed with $[Ag_{44}(SR)_{30}]^{4-}$ in DMF to allow the self-assembly of Ag_{44} NCs into a superstructure encapsulating a single GNR in each nanocomposite. The self-assembly was proposed to be directed by H-bonding formed between the *p*-MBA ligands bound on both Ag_{44} and GNR.[114]

4.4. Ligand Interactions in Binary Assembly. The assembly of two different types of NPs into binary superlattices (BNSLs) provides a versatile way to obtain artificially made materials with precisely controlled chemical composition and periodic placement of each component. To date, dozens of BNSLs have been reported,[97,120−122] for example, the hexagonal AB_2 superlattice (isostructural with AlB_2) assembled from 11.5 nm Fe_2O_3 and 6.1 nm Au NPs.[123] Calculations on hard-sphere models show that the assembly of hard spheres into BNSLs isostructural with NaCl, AlB_2, and $NaZn_{13}$ structures can be entropy-driven.[124] Other factors, including van der Waals, electrostatic, and directional dipolar interactions as well as steric repulsion, can also contribute to the inter-NP potential.[18,125−127]

In the atomically precise BNSL reported by the Zheng group, the 3.3 nm (including the thickness of ligand shell) $Au_{267-x}Ag_x(SR)_{80}$ and 2.1 × 2.5 nm $Au_{45-x}Ag_x(SR)_{27}(PPh_3)_6$ (SR = $SPh(CH_3)_2$) NCs are co-crystallized into a hexagonal superlattice with a 1:1 ratio (Figure 14a), being isostructural with PtB, which is predicted to have an effective size ratio γ (R_{small}/R_{large}) of ∼0.4.[128] However, in the hierarchical assembly, the BNSL of $Au_{267-x}Ag_x(SR)_{80}$ and $Au_{45-x}Ag_x(SR)_{27}(PPh_3)_6$ NCs shows γ as high as 0.64−0.76, indicating much stronger interactions between the ligands of the NCs. The small $Au_{45-x}Ag_x(SR)_{27}(PPh_3)_6$ NP is coordinated by anisotropically distributed thiolates and phosphines, and each $Au_{45-x}Ag_x(SR)_{27}(PPh_3)_6$ NP is neighbored by six large $Au_{267-x}Ag_x(SR)_{80}$ NCs along the directions of its six phosphine ligands, resulting in a centered trigonal prism (Figure 14b). The three pairs of interacting ligands, i.e., one PPh_3 ligand of $Au_{45-x}Ag_x(SR)_{27}(PPh_3)_6$ and three thiolates of $Au_{267-x}Ag_x(SR)_{80}$, form a "socket-plug" match via the C−H···π interactions (Figure 14c). In total, six of such "diblock" conformations on the periphery of a $Au_{45-x}Ag_x(SR)_{27}(PPh_3)_6$

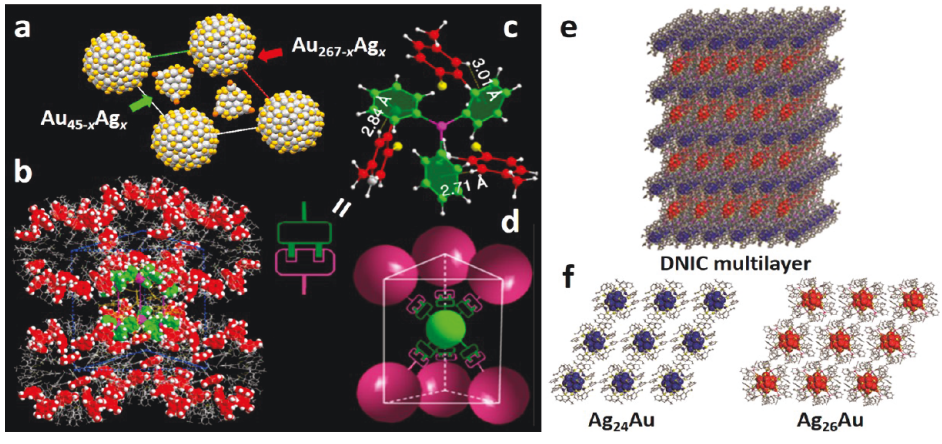

Figure 14. (a) Hexagonal unit cell of the co-crystal structure of $Au_{267-x}Ag_x(SR)_{80}$ and $Au_{45-x}Ag_x(SR)_{27}(PPh_3)_6$ NCs viewed down the *z*-axis. (b) Arrangements of surface ligands on both $Au_{267-x}Ag_x(SR)_{80}$ (the C atoms are marked in red) and $Au_{45-x}Ag_x6(SR)_{27}(PPh_3)_6$ (the C atoms are marked in green). (c) The C−H···π interactions between the thiolates on $Au_{267-x}Ag_x(SR)_{80}$ and the phosphines on $Au_{45-x}Ag_x(SR)_{27}(PPh_3)_6$, resembling a "socket-plug" match. (d) Scheme of the anisotropic packing in BNSL. (e) The self-assembly packing of $[Ag_{24}Au(SR)_{18}]^-$ and $[Ag_{26}Au(SR)_{18}(PPh_3)_6]^+$ into a DNIC multilayer structure. (f) Individual layers of $[Ag_{24}Au(SR)_{18}]^-$ and $[Ag_{26}Au(SR)_{18}(PPh_3)_6]^+$. Panel a is redrawn from ref 128. Panels b−d are reproduced with permission from ref 128. Copyright 2018 Springer Nature and distributed under the terms of the Creative Commons CC BY license. Panels e and f are reproduced with permission from ref 129. Copyright 2019 Wiley-VCH Verlag GmbH & Co. KGaA, Weinheim.

https://dx.doi.org/10.1021/jacs.0c05866
J. Am. Chem. Soc. 2020, 142, 13627−13644

NC (Figure 14d) lead to packing constraints and further generate the intriguing and unconventional BNSL.[128]

The co-assembly of anionic $[Ag_{24}Au(SR)_{18}]^-$ and cationic $[Ag_{26}Au(SR)_{18}(PPh_3)_6]^+$ (SR = *o*-ethylbenzenethiolate) NCs into a superlattice (Figure 14e) results in a double nanocluster ion compound (DNIC).[129] In the DNIC, every layer is a hcp packing of pure $[Ag_{24}Au(SR)_{18}]^-$ or $[Ag_{26}Au(SR)_{18}(PPh_3)_6]^+$ NCs (Figure 14f), and such layers then alternately stack up along the [001] direction. Beside the electrostatic interactions between the NCs with opposite charges, both ends of each rod-shaped $[Ag_{26}Au(SR)_{18}(PPh_3)_6]^+$ NP might also be connected with four $[Ag_{24}Au(SR)_{18}]^-$ NCs in neighboring layers (layers above and below) via C−H···π, π···π, and H···H interactions.[129]

5. CONCLUSION AND OUTLOOK

By the synthesis of atomically precise NPs and with the help of SCXRD, the total structures of small-sized NPs can now be achieved. Atomic resolution for the ligand interactions in the ligand shell is achieved and illustrated, and similarly the interactions between NPs that further direct the self-assembly of NPs into coherent superlattices. Interesting patterns due to the ligand assembly, e.g., herringbone patterns, rotational patterns, and chiral patterns, are discovered. These details are indeed enlightening to the fields beyond nanochemistry; for example, to the nanomedicine field, in how the ligand-protected NPs interact with proteins and cell membranes at the molecular level;[5,6,130,131] to the heterogeneous catalysis field, in how the ligand-protected NPs control the substrate conformation for catalysis;[132] and to the quantum field, in how the quantum states and spins in atomically precise NP superlattices[133] can be manipulated for coherent operations.

Ligand-protected NPs assemble into superstructures that are dependent on the NP uniformity, shape, and surface ligands. The assembly can be driven by entropy as well as van der Waals forces, dipolar interactions, electrostatic forces, steric repulsion, etc., among which ligands play the most significant roles in directing the alignment of NPs. Starting from the primary structure of ligands, interactions between them lead to secondary structures in the ligand shell on the particle surface, and further interactions between the ligand patterns of neighboring NPs result in tertiary structures, i.e., the hierarchical superstructures.

The major challenge of obtaining information on ligand interactions on large-sized, atomically precise NPs (e.g., core size of hundreds of atoms) still lies in the growth of high-quality single crystals. Despite the experimental difficulties, we expect the following work to be done in the future. (1) The ligand interactions should not be limited to those between individual ligands on NPs, or at the corresponding parts of two approaching NPs. Collective interactions among the ligands, and even among the ligand shells of NPs, would be more insightful in implying the emergence of collective properties for self-assembled superlattices. For example, the herringbone pattern formed in the coherent superlattice of $Au_{103}S_2(SR)_{41}$ NCs is more likely to bring about new collective properties. (2) Although the strong π···π stacking and H-bonds and the weak H···H interactions have been demonstrated, what is in-between (i.e., dipole−dipole interaction with energy lying between the two regimes) has not been adequately explored yet, and the dipole moment achieved by ligand assembly for anisotropic NPs is worth studying in future work. (3) Most of the ligand interactions discussed so far focus on attraction; however, more attention should be paid to the details of repulsive forces, e.g., steric repulsion and charge-involved electrostatic repulsion, as these are also critical in determining the alignment of ligands in the shell as well as the interacting ligand shells. (4) It remains unclear how the Au(111), (110), and high-index facets of NPs are stabilized by thiolate ligands, although the Au(100) stabilization has been clear owing to the successful crystallization of the $Au_{92}(SR)_{44}$ NC with sufficiently large (100) facets. This calls for future breakthroughs in crystallization of NCs with sufficient Au(111) facets exposed. Theoretical modeling[134−138] on large-sized NCs and intriguing electronic properties[139−142] also remains to be pursued. (5) The collective properties, such as the optical, mechanical, and piezoelectric properties, as well as the electric and thermal conductivity of atomically precise superlattices in which the NPs are connected by coherent intra- and inter-NP ligand interactions are awaiting to be studied. Overall, the advent of atomically precise nanoparticles will provide many exciting opportunities in future research.

AUTHOR INFORMATION

Corresponding Author

Rongchao Jin − *Department of Chemistry, Carnegie Mellon University, Pittsburgh, Pennsylvania 15213, United States;* orcid.org/0000-0002-2525-8345; Email: rongchao@andrew.cmu.edu

Author

Yingwei Li − *Department of Chemistry, Carnegie Mellon University, Pittsburgh, Pennsylvania 15213, United States*

Complete contact information is available at: https://pubs.acs.org/10.1021/jacs.0c05866

Notes

The authors declare no competing financial interest.

ACKNOWLEDGMENTS

R.J. acknowledges the National Science Foundation (DMR-1808675) and Air Force Office of Scientific Research for financial support.

REFERENCES

(1) Jin, R.; Cao, Y. W.; Mirkin, C. A.; Kelly, K. L.; Schatz, G. C.; Zheng, J. G. Photoinduced Conversion of Silver Nanospheres to Nanoprisms. *Science* **2001**, *294*, 1901−1903.

(2) Sun, Y.; Xia, Y. Shape-Controlled Synthesis of Gold and Silver Nanoparticles. *Science* **2002**, *298*, 2176−2179.

(3) Tao, A. R.; Habas, S.; Yang, P. Shape Control of Colloidal Metal Nanocrystals. *Small* **2008**, *4*, 310−325.

(4) Grzelczak, M.; Pérez-Juste, J.; Mulvaney, P.; Liz-Marzán, L. M. Shape Control in Gold Nanoparticle Synthesis. *Chem. Soc. Rev.* **2008**, *37*, 1783−1791.

(5) Murphy, C. J.; Chang, H.-H.; Falagan-Lotsch, P.; Gole, M. T.; Hofmann, D. M.; Hoang, K. N. L.; Meyer, S. M.; McClain, S. M.; Turner, J. G.; Unnikrishnan, M.; Wu, M.; Zhang, X.; Zhang, Y. Virus-Sized Gold Nanorods: Plasmonic Particles for Biology. *Acc. Chem. Res.* **2019**, *52*, 2124−2135.

(6) Ong, Q.; Luo, Z.; Stellacci, F. Characterization of Ligand Shell for Mixed-Ligand Coated Gold Nanoparticles. *Acc. Chem. Res.* **2017**, *50*, 1911−1919.

(7) Jackson, A. M.; Hu, Y.; Silva, P. J.; Stellacci, F. From Homoligand- to Mixed-Ligand-Monolayer-Protected Metal Nanoparticles: A Scanning Tunneling Microscopy Investigation. *J. Am. Chem. Soc.* **2006**, *128*, 11135−11149.

(8) Sologan, M.; Marson, D.; Polizzi, S.; Pengo, P.; Boccardo, S.; Pricl, S.; Posocco, P.; Pasquato, L. Patchy and Janus Nanoparticles by Self-Organization of Mixtures of Fluorinated and Hydrogenated Alkanethiolates on the Surface of a Gold Core. *ACS Nano* **2016**, *10*, 9316−9325.
(9) Farrell, Z.; Merz, S.; Seager, J.; Dunn, C.; Egorov, S.; Green, D. L. Development of Experiment and Theory to Detect and Predict Ligand Phase Separation on Silver Nanoparticles. *Angew. Chem., Int. Ed.* **2015**, *54*, 6479−6482.
(10) Whetten, R. L.; Shafigullin, M. N.; Khoury, J. T.; Schaaff, T. G.; Vezmar, I.; Alvarez, M. M.; Wilkinson, A. Crystal Structures of Molecular Gold Nanocrystal Arrays. *Acc. Chem. Res.* **1999**, *32*, 397−406.
(11) Lin, X. M.; Jaeger, H. M.; Sorensen, C. M.; Klabunde, K. J. Formation of Long-Range-Ordered Nanocrystal Superlattices on Silicon Nitride Substrates. *J. Phys. Chem. B* **2001**, *105*, 3353−3357.
(12) Grzelczak, M.; Vermant, J.; Furst, E. M.; Liz-Marzán, L. M. Directed Self-Assembly of Nanoparticles. *ACS Nano* **2010**, *4*, 3591−3605.
(13) Nie, Z.; Petukhova, A.; Kumacheva, E. Properties and Emerging Applications of Self-Assembled Structures Made from Inorganic Nanoparticles. *Nat. Nanotechnol.* **2010**, *5*, 15−25.
(14) Wang, T.; Zhuang, J.; Lynch, J.; Chen, O.; Wang, Z.; Wang, X.; LaMontagne, D.; Wu, H.; Wang, Z.; Cao, Y. C. Self-Assembled Colloidal Superparticles from Nanorods. *Science* **2012**, *338*, 358−363.
(15) Nagaoka, Y.; Zhu, H.; Eggert, D.; Chen, O. Single-Component Quasicrystalline Nanocrystal Superlattices through Flexible Polygon Tiling Rule. *Science* **2018**, *362*, 1396−1400.
(16) Stoeva, S. I.; Prasad, B. L. V.; Uma, S.; Stoimenov, P. K.; Zaikovski, V.; Sorensen, C. M.; Klabunde, K. J. Face-Centered Cubic and Hexagonal Closed-Packed Nanocrystal Superlattices of Gold Nanoparticles Prepared by Different Methods. *J. Phys. Chem. B* **2003**, *107*, 7441−7448.
(17) Murray, C. B.; Kagan, C. R.; Bawendi, M. G. Synthesis and Characterization of Monodisperse Nanocrystals and Close-Packed Nanocrystal Assemblies. *Annu. Rev. Mater. Sci.* **2000**, *30*, 545−610.
(18) Sharma, J.; Chhabra, R.; Cheng, A.; Brownell, J.; Liu, Y.; Yan, H. Control of Self-Assembly of DNA Tubules Through Integration of Gold Nanoparticles. *Science* **2009**, *323*, 112−116.
(19) Yi, C.; Zhang, S.; Webb, K. T.; Nie, Z. Anisotropic Self-Assembly of Hairy Inorganic Nanoparticles. *Acc. Chem. Res.* **2017**, *50*, 12−21.
(20) Jin, R.; Zeng, C.; Zhou, M.; Chen, Y. Atomically Precise Colloidal Metal Nanoclusters and Nanoparticles: Fundamentals and Opportunities. *Chem. Rev.* **2016**, *116*, 10346−10413.
(21) Yao, Q.; Yuan, X.; Chen, T.; Leong, D. T.; Xie, J. Engineering Functional Metal Materials at the Atomic Level. *Adv. Mater.* **2018**, *30*, 1802751.
(22) Yan, J.; Teo, B. K.; Zheng, N. Surface Chemistry of Atomically Precise Coinage-Metal Nanoclusters: From Structural Control to Surface Reactivity and Catalysis. *Acc. Chem. Res.* **2018**, *51*, 3084−3093.
(23) Lei, Z.; Wan, X.-K.; Yuan, S.-F.; Guan, Z.-J.; Wang, Q.-M. Alkynyl Approach toward the Protection of Metal Nanoclusters. *Acc. Chem. Res.* **2018**, *51*, 2465−2474.
(24) Higaki, T.; Li, Q.; Zhou, M.; Zhao, S.; Li, Y.; Li, S.; Jin, R. Toward the Tailoring Chemistry of Metal Nanoclusters for Enhancing Functionalities. *Acc. Chem. Res.* **2018**, *51*, 2764−2773.
(25) Tian, S.; Li, Y.-Z.; Li, M.-B.; Yuan, J.; Yang, J.; Wu, Z.; Jin, R. Structural Isomerism in Gold Nanoparticles Revealed by X-Ray Crystallography. *Nat. Commun.* **2015**, *6*, 8667.
(26) Sharma, S.; Chakrahari, K. K.; Saillard, J.-Y.; Liu, C. W. Structurally Precise Dichalcogenolate-Protected Copper and Silver Superatomic Nanoclusters and Their Alloys. *Acc. Chem. Res.* **2018**, *51*, 2475−2483.
(27) Wang, S.; Li, Q.; Kang, X.; Zhu, M. Customizing the Structure, Composition, and Properties of Alloy Nanoclusters by Metal Exchange. *Acc. Chem. Res.* **2018**, *51*, 2784−2792.
(28) Sakthivel, N. A.; Dass, A. Aromatic Thiolate-Protected Series of Gold Nanomolecules and a Contrary Structural Trend in Size Evolution. *Acc. Chem. Res.* **2018**, *51*, 1774−1783.
(29) Schoenbaum, C. A.; Schwartz, D. K.; Medlin, J. W. Controlling the Surface Environment of Heterogeneous Catalysts Using Self-Assembled Monolayers. *Acc. Chem. Res.* **2014**, *47*, 1438−1445.
(30) Li, Y.; Chen, Y.; House, S. D.; Zhao, S.; Wahab, Z.; Yang, J. C.; Jin, R. Interface Engineering of Gold Nanoclusters for CO Oxidation Catalysis. *ACS Appl. Mater. Interfaces* **2018**, *10*, 29425−29434.
(31) Knoppe, S.; Bürgi, T. Chirality in Thiolate-protected Gold Clusters. *Acc. Chem. Res.* **2014**, *47*, 1318−1326.
(32) Li, Y.; Higaki, T.; Du, X.; Jin, R. Chirality and Surface Bonding Correlation in Atomically Precise Metal Nanoclusters. *Adv. Mater.* **2020**, 1905488.
(33) Ong, W.-L.; O'Brien, E. S.; Dougherty, P. S. M.; Paley, D. W.; Higgs, C. F., III; McGaughey, A. J. H.; Malen, J. A.; Roy, X. Orientational Order Controls Crystalline and Amorphous Thermal Transport in Superatomic Crystals. *Nat. Mater.* **2017**, *16*, 83−88.
(34) Choi, B.; Yu, J.; Paley, D. W.; Trinh, M. T.; Paley, M. V.; Karch, J. M.; Crowther, A. C.; Lee, C.-H.; Lalancette, R. A.; Zhu, X.; Kim, P.; Steigerwald, M. L.; Nuckolls, C.; Roy, X. Van Der Waals Solids from Self-Assembled Nanoscale Building Blocks. *Nano Lett.* **2016**, *16*, 1445−1449.
(35) Turkiewicz, A.; Paley, D. W.; Besara, T.; Elbaz, G.; Pinkard, A.; Siegrist, T.; Roy, X. Assembling Hierarchical Cluster Solids with Atomic Precision. *J. Am. Chem. Soc.* **2014**, *136*, 15873−15876.
(36) Hernández Sánchez, R.; Champsaur, A. M.; Choi, B.; Wang, S. G.; Bu, W.; Roy, X.; Chen, Y.-S.; Steigerwald, M. L.; Nuckolls, C.; Paley, D. W. Electron Cartography in Clusters. *Angew. Chem., Int. Ed.* **2018**, *57*, 13815−13820.
(37) Pinkard, A.; Champsaur, A. M.; Roy, X. Molecular Clusters: Nanoscale Building Blocks for Solid-State Materials. *Acc. Chem. Res.* **2018**, *51*, 919−929.
(38) Nonappa; Ikkala, O. Hydrogen Bonding Directed Colloidal Self-Assembly of Nanoparticles into 2D Crystals, Capsids, and Supracolloidal Assemblies. *Adv. Funct. Mater.* **2018**, *28*, 1704328.
(39) Chakraborty, P.; Nag, A.; Chakraborty, A.; Pradeep, T. Approaching Materials with Atomic Precision Using Supramolecular Cluster Assemblies. *Acc. Chem. Res.* **2019**, *52*, 2−11.
(40) Kang, X.; Zhu, M. Intra-Cluster Growth Meets Inter-Cluster Assembly the Molecular and Supramolecular Chemistry of Atomically Precise Nanoclusters. *Coord. Chem. Rev.* **2019**, *394*, 1−38.
(41) Zeng, C.; Chen, Y.; Kirschbaum, K.; Lambright, K. J.; Jin, R. Emergence of Hierarchical Structural Complexities in Nanoparticles and Their Assembly. *Science* **2016**, *354*, 1580−1584.
(42) Yan, N.; Xia, N.; Liao, L.; Zhu, M.; Jin, F.; Jin, R.; Wu, Z. Unraveling the Long-Pursued Au_{144} Structure by X-Ray Crystallography. *Sci. Adv.* **2018**, *4*, No. eaat7259.
(43) Song, Y.; Li, Y.; Li, H.; Ke, F.; Xiang, J.; Zhou, C.; Li, P.; Zhu, M.; Jin, R. Atomically Resolved $Au_{52}Cu_{72}(SR)_{55}$ Nanoalloy Reveals Marks Decahedron Truncation and Penrose Tiling Surface. *Nat. Commun.* **2020**, *11*, 478.
(44) Zhu, M.; Aikens, C. M.; Hollander, F. J.; Schatz, G. C.; Jin, R. Correlating the Crystal Structure of a Thiol-Protected Au_{25} Cluster and Optical Properties. *J. Am. Chem. Soc.* **2008**, *130*, 5883−5885.
(45) Li, G.; Abroshan, H.; Liu, C.; Zhuo, S.; Li, Z.; Xie, Y.; Kim, H. J.; Rosi, N. L.; Jin, R. Tailoring the Electronic and Catalytic Properties of Au_{25} Nanoclusters via Ligand Engineering. *ACS Nano* **2016**, *10*, 7998−8005.
(46) Joshi, C. P.; Bootharaju, M. S.; Alhilaly, M. J.; Bakr, O. M. $[Ag_{25}(SR)_{18}]^-$: The "Golden" Silver Nanoparticle. *J. Am. Chem. Soc.* **2015**, *137*, 11578−11581.
(47) Li, J.-J.; Guan, Z.-J.; Lei, Z.; Hu, F.; Wang, Q.-M. Same Magic Number but Different Arrangement: Alkynyl-Protected Au_{25} with D_3 Symmetry. *Angew. Chem., Int. Ed.* **2019**, *58*, 1083−1087.
(48) Gunawardene, P. N.; Corrigan, J. F.; Workentin, M. S. Golden Opportunity: A Clickable Azide-Functionalized $[Au_{25}(SR)_{18}]^-$ Nanocluster Platform for Interfacial Surface Modifications. *J. Am. Chem. Soc.* **2019**, *141*, 11781−11785.

https://dx.doi.org/10.1021/jacs.0c05866
J. Am. Chem. Soc. 2020, 142, 13627−13644

(49) Kauffman, D. R.; Alfonso, D.; Matranga, C.; Qian, H.; Jin, R. Experimental and Computational Investigation of Au_{25} Clusters and CO_2: A Unique Interaction and Enhanced Electrocatalytic Activity. *J. Am. Chem. Soc.* **2012**, *134*, 10237−10243.
(50) Jung, J.; Kang, S.; Han, Y.-K. Ligand Effects on the Stability of Thiol-Stabilized Gold Nanoclusters: $Au_{25}(SR)_{18}^{-}$, $Au_{38}(SR)_{24}$, and $Au_{102}(SR)_{44}$. *Nanoscale* **2012**, *4*, 4206−4210.
(51) Negishi, Y.; Iwai, T.; Ide, M. Continuous Modulation of Electronic Structure of Stable Thiolate-Protected Au_{25} Cluster by Ag Doping. *Chem. Commun.* **2010**, *46*, 4713−4715.
(52) Kauffman, D. R.; Alfonso, D.; Matranga, C.; Qian, H.; Jin, R. A Quantum Alloy: The Ligand-Protected $Au_{25-x}Ag_x(SR)_{18}$ Cluster. *J. Phys. Chem. C* **2013**, *117*, 7914−7923.
(53) Kumara, C.; Aikens, C. M.; Dass, A. X-Ray Crystal Structure and Theoretical Analysis of $Au_{25-x}Ag_x(SCH_2CH_2Ph)_{18}^{-}$ Alloy. *J. Phys. Chem. Lett.* **2014**, *5*, 461−466.
(54) Bootharaju, M. S.; Joshi, C. P.; Parida, M. R.; Mohammed, O. F.; Bakr, O. M. Templated Atom-Precise Galvanic Synthesis and Structure Elucidation of a $[Ag_{24}Au(SR)_{18}]^{-}$ Nanocluster. *Angew. Chem.* **2016**, *128*, 934−938.
(55) Li, Q.; Wang, S.; Kirschbaum, K.; Lambright, K. J.; Das, A.; Jin, R. Heavily Doped $Au_{25-x}Ag_x(SC_6H_{11})_{18}^{-}$ Nanoclusters: Silver Goes from the Core to the Surface. *Chem. Commun.* **2016**, *52*, 5194−5197.
(56) Zhu, M.; Eckenhoff, W. T.; Pintauer, T.; Jin, R. Conversion of Anionic $[Au_{25}(SCH_2CH_2Ph)_{18}]^{-}$ Cluster to Charge Neutral Cluster via Air Oxidation. *J. Phys. Chem. C* **2008**, *112*, 14221−14224.
(57) Tofanelli, M. A.; Salorinne, K.; Ni, T. W.; Malola, S.; Newell, B.; Phillips, B.; Häkkinen, H.; Ackerson, C. J. Jahn-Teller Effects in $Au_{25}(SR)_{18}$. *Chem. Sci.* **2016**, *7*, 1882−1890.
(58) Ni, T. W.; Tofanelli, M. A.; Phillips, B. D.; Ackerson, C. J. Structural Basis for Ligand Exchange on $Au_{25}(SR)_{18}$. *Inorg. Chem.* **2014**, *53*, 6500−6502.
(59) Dou, R.-F.; Ma, X.-C.; Xi, L.; Yip, H. L.; Wong, K. Y.; Lau, W. M.; Jia, J.-F.; Xue, Q.-K.; Yang, W.-S.; Ma, H.; Jen, A. K.-Y. Self-Assembled Monolayers of Aromatic Thiols Stabilized by Parallel-Displaced π-π Stacking Interactions. *Langmuir* **2006**, *22*, 3049−3056.
(60) Zeng, C.; Qian, H.; Li, T.; Li, G.; Rosi, N. L.; Yoon, B.; Barnett, R. N.; Whetten, R. L.; Landman, U.; Jin, R. Total Structure and Electronic Properties of the Gold Nanocrystal $Au_{36}(SR)_{24}$. *Angew. Chem., Int. Ed.* **2012**, *51*, 13114−13118.
(61) Chen, Y.; Liu, C.; Tang, Q.; Zeng, C.; Higaki, T.; Das, A.; Jiang, D.-e.; Rosi, N. L.; Jin, R. Isomerism in $Au_{28}(SR)_{20}$ Nanocluster and Stable Structures. *J. Am. Chem. Soc.* **2016**, *138*, 1482−1485.
(62) Zeng, C.; Chen, Y.; Iida, K.; Nobusada, K.; Kirschbaum, K.; Lambright, K. J.; Jin, R. Gold Quantum Boxes: On the Periodicities and the Quantum Confinement in the Au_{28}, Au_{36}, Au_{44}, and Au_{52} Magic Series. *J. Am. Chem. Soc.* **2016**, *138*, 3950−3953.
(63) Zeng, C.; Liu, C.; Chen, Y.; Rosi, N. L.; Jin, R. Atomic Structure of Self-Assembled Monolayer of Thiolates on a Tetragonal Au_{92} Nanocrystal. *J. Am. Chem. Soc.* **2016**, *138*, 8710−8713.
(64) Qian, H.; Eckenhoff, W. T.; Zhu, Y.; Pintauer, T.; Jin, R. Total Structure Determination of Thiolate-Protected Au38 Nanoparticles. *J. Am. Chem. Soc.* **2010**, *132*, 8280−8281.
(65) Zeng, C.; Chen, Y.; Kirschbaum, K.; Appavoo, K.; Sfeir, M. Y.; Jin, R. Structural Patterns at All Scales in a Nonmetallic Chiral $Au_{133}(SR)_{52}$ Nanoparticle. *Sci. Adv.* **2015**, *1*, No. e1500045.
(66) Das, A.; Li, T.; Nobusada, K.; Zeng, C.; Rosi, N. L.; Jin, R. Nonsuperatomic $[Au_{23}(SC_6H_{11})_{16}]^{-}$ Nanocluster Featuring Bipyramidal Au_{15} Kernel and Trimeric $Au_3(SR)_4$ Motif. *J. Am. Chem. Soc.* **2013**, *135*, 18264−18267.
(67) Zeng, C.; Li, T.; Das, A.; Rosi, N. L.; Jin, R. Chiral Structure of Thiolate-Protected 28-Gold-Atom Nanocluster Determined by X-Ray Crystallography. *J. Am. Chem. Soc.* **2013**, *135*, 10011−10013.
(68) Zeng, C.; Chen, Y.; Liu, C.; Nobusada, K.; Rosi, N. L.; Jin, R. Gold Tetrahedra Coil up: Kelulé-Like and Double Helical Superstructures. *Sci. Adv.* **2015**, *1*, No. e1500425.
(69) Higaki, T.; Zhou, M.; Lambright, K. J.; Kirschbaum, K.; Sfeir, M. Y.; Jin, R. Sharp Transition from Nonmetallic Au_{246} to Metallic Au_{279} with Nascent Surface Plasmon Resonance. *J. Am. Chem. Soc.* **2018**, *140*, 5691−5695.
(70) Jadzinsky, P. D.; Calero, G.; Ackerson, C. J.; Bushnell, D. A.; Kornberg, R. D. Structure of a Thiol Monolayer-Protected Gold Nanoparticle at 1.1 Å Resolution. *Science* **2007**, *318*, 430−433.
(71) Higaki, T.; Liu, C.; Zhou, M.; Luo, T.-Y.; Rosi, N. L.; Jin, R. Tailoring the Structure of 58-Electron Gold Nanoclusters: $Au_{103}S_2(S\text{-}Nap)_{41}$ and Its Implications. *J. Am. Chem. Soc.* **2017**, *139*, 9994−10001.
(72) Chen, Y.; Zeng, C.; Liu, C.; Kirschbaum, K.; Gayathri, C.; Gil, R. R.; Rosi, N. L.; Jin, R. Crystal Structure of Barrel-Shaped Chiral $Au_{130}(p\text{-}MBT)_{50}$ Nanocluster. *J. Am. Chem. Soc.* **2015**, *137*, 10076−10079.
(73) Liu, C.; Li, T.; Li, G.; Nobusada, K.; Zeng, C.; Pang, G.; Rosi, N. L.; Jin, R. Observation of Body-Centered Cubic Gold Nanocluster. *Angew. Chem., Int. Ed.* **2015**, *54*, 9826−9829.
(74) Higaki, T.; Liu, C.; Zeng, C.; Jin, R.; Chen, Y.; Rosi, N. L.; Jin, R. Controlling the Atomic Structure of Au30 Nanoclusters by a Ligand-Based Strategy. *Angew. Chem., Int. Ed.* **2016**, *55*, 6694−6697.
(75) Liao, L.; Zhuang, S.; Wang, P.; Xu, Y.; Yan, N.; Dong, H.; Wang, C.; Zhao, Y.; Xia, N.; Li, J.; Deng, H.; Pei, Y.; Tian, S.-K.; Wu, Z. Quasi-Dual-Packed-Kerneled $Au_{49}(2,4\text{-}DMBT)_{27}$ Nanoclusters and the Influence of Kernel Packing on the Electrochemical Gap. *Angew. Chem., Int. Ed.* **2017**, *56*, 12644−12648.
(76) Wan, L.-J.; Terashima, M.; Noda, H.; Osawa, M. Molecular Orientation and Ordered Structure of Benzenethiol Adsorbed on Gold(111). *J. Phys. Chem. B* **2000**, *104*, 3563−3569.
(77) Vericat, C.; Vela, M. E.; Salvarezza, R. C. Self-Assembled Monolayers of Alkanethiols on Au(111): Surface Structures, Defects and Dynamics. *Phys. Chem. Chem. Phys.* **2005**, *7*, 3258−3268.
(78) Nishio, M. The CH−π Hydrogen Bonds in Biological Macromolecules. *Phys. Chem. Chem. Phys.* **2011**, *13*, 13873−13900.
(79) Ren, L.; Yuan, P.; Su, H.; Malola, S.; Lin, S.; Tang, Z.; Teo, B. K.; Häkkinen, H.; Zheng, L.; Zheng, N. Bulky Surface Ligands Promote Surface Reactivities of $[Ag_{141}X_{12}(S\text{-}Adm)_{40}]^{3+}$ (X = Cl, Br, I) Nanoclusters: Models for Multiple-Twinned Nanoparticles. *J. Am. Chem. Soc.* **2017**, *139*, 13288−13291.
(80) Yang, H.; Wang, Y.; Chen, X.; Zhao, X.; Gu, L.; Huang, H.; Yan, J.; Xu, C.; Li, G.; Wu, J.; Edwards, A. J.; Dittrich, B.; Tang, Z.; Wang, D.; Lehtovaara, L.; Häkkinen, H.; Zheng, N. Plasmonic Twinned Silver Nanoparticles with Molecular Precision. *Nat. Commun.* **2016**, *7*, 12809.
(81) Jackson, A. M.; Myerson, J. W.; Stellacci, F. Spontaneous Assembly of Subnanometre-Ordered Domains in the Ligand Shell of Monolayer-Protected Nanoparticles. *Nat. Mater.* **2004**, *3*, 330−336.
(82) Cowan, M. J.; Higaki, T.; Jin, R.; Mpourmpakis, G. Understanding the Solubility Behavior of Atomically Precise Gold Nanoclusters. *J. Phys. Chem. C* **2019**, *123*, 20006−20012.
(83) Li, Y.; Luo, T.-Y.; Zhou, M.; Song, Y.; Rosi, N. L.; Jin, R. A Correlated Series of Au/Ag Nanoclusters Revealing the Evolutionary Patterns of Asymmetric Ag Doping. *J. Am. Chem. Soc.* **2018**, *140*, 14235−14243.
(84) Li, Y.; Cowan, M. J.; Zhou, M.; Taylor, M. G.; Wang, H.; Song, Y.; Mpourmpakis, G.; Jin, R. Heterometal-Doped M_{23} (M = Au/Ag/Cd) Nanoclusters with Large Dipole Moments. *ACS Nano* **2020**, *14*, 6599−6606.
(85) Talapin, D. V.; Lee, J.-S.; Kovalenko, M. V.; Shevchenko, E. V. Prospects of Colloidal Nanocrystals for Electronic and Optoelectronic Applications. *Chem. Rev.* **2010**, *110*, 389−458.
(86) Boles, M. A.; Engel, M.; Talapin, D. V. Self-Assembly of Colloidal Nanocrystals: From Intricate Structures to Functional Materials. *Chem. Rev.* **2016**, *116*, 11220−11289.
(87) Stupp, S. I.; LeBonheur, V.; Walker, K.; Li, L. S.; Huggins, K. E.; Keser, M.; Amstutz, A. Supramolecular Materials: Self-Organized Nanostructures. *Science* **1997**, *276*, 384−389.
(88) Boal, A. K.; Ilhan, F.; DeRouchey, J. E.; Thurn-Albrecht, T.; Russell, T.; Rotello, V. M. Self-Assembly of Nanoparticles into Structured Spherical and Network Aggregates. *Nature* **2000**, *404*, 746−748.

https://dx.doi.org/10.1021/jacs.0c05866
J. Am. Chem. Soc. 2020, 142, 13627−13644

(89) Lim, S. I.; Zhong, C.-J. Molecularly Mediated Processing and Assembly of Nanoparticles: Exploring the Interparticle Interactions and Structures. *Acc. Chem. Res.* **2009**, *42*, 798−808.
(90) Nagaoka, Y.; Tan, R.; Li, R.; Zhu, H.; Eggert, D.; Wu, Y. A.; Liu, Y.; Wang, Z.; Chen, O. Superstructures Generated from Truncated Tetrahedral Quantum Dots. *Nature* **2018**, *561*, 378−382.
(91) Boneschanscher, M. P.; Evers, W. H.; Geuchies, J. J.; Altantzis, T.; Goris, B.; Rabouw, F. T.; van Rossum, S. A. P.; van der Zant, H. S. J.; Siebbeles, L. D. A.; Van Tendeloo, G.; Swart, I.; Hilhorst, J.; Petukhov, A. V.; Bals, S.; Vanmaekelbergh, D. Long-Range Orientation and Atomic Attachment of Nanocrystals in 2D Honeycomb Superlattices. *Science* **2014**, *344*, 1377−1380.
(92) Lin, H.; Lee, S.; Sun, L.; Spellings, M.; Engel, M.; Glotzer, S. C.; Mirkin, C. A. Clathrate Colloidal Crystals. *Science* **2017**, *355*, 931−935.
(93) Li, Q.; Russell, J. C.; Luo, T.-Y.; Roy, X.; Rosi, N. L.; Zhu, Y.; Jin, R. Modulating the Hierarchical Fibrous Assembly of Au Nanoparticles with Atomic Precision. *Nat. Commun.* **2018**, *9*, 3871.
(94) AbdulHalim, L. G.; Bootharaju, M. S.; Tang, Q.; Del Gobbo, S.; AbdulHalim, R. G.; Eddaoudi, M.; Jiang, D.-e.; Bakr, O. M. $Ag_{29}(BDT)_{12}(TPP)_4$: A Tetravalent Nanocluster. *J. Am. Chem. Soc.* **2015**, *137*, 11970−11975.
(95) Nag, A.; Chakraborty, P.; Bodiuzzaman, M.; Ahuja, T.; Antharjanam, S.; Pradeep, T. Polymorphism of $Ag_{29}(BDT)_{12}(TPP)_4^{3-}$ Cluster Interactions of Secondary Ligands and Their Effect on Solid State Luminescence. *Nanoscale* **2018**, *10*, 9851−9855.
(96) Shevchenko, E. V.; Talapin, D. V.; O'Brien, S.; Murray, C. B. Polymorphism in AB_{13} Nanoparticle Superlattices An Example of Semiconductor-Metal Metamaterials. *J. Am. Chem. Soc.* **2005**, *127*, 8741−8747.
(97) Ye, X.; Chen, J.; Murray, C. B. Polymorphism in Self-Assembled AB_6 Binary Nanocrystal Superlattices. *J. Am. Chem. Soc.* **2011**, *133*, 2613−2620.
(98) Sun, S.; Murray, C. B.; Weller, D.; Folks, L.; Moser, A. Monodisperse FePt Nanoparticles and Ferromagnetic FePt Nanocrystal Superlattices. *Science* **2000**, *287*, 1989−1992.
(99) De Nardi, M.; Antonello, S.; Jiang, D.-e.; Pan, F.; Rissanen, K.; Ruzzi, M.; Venzo, A.; Zoleo, A.; Maran, F. Gold Nanowired: A Linear $(Au_{25})_n$ Polymer from Au_{25} Molecular Clusters. *ACS Nano* **2014**, *8*, 8505−8512.
(100) Dainese, T.; Antonello, S.; Gascón, J. A.; Pan, F.; Perera, N. V.; Ruzzi, M.; Venzo, A.; Zoleo, A.; Rissanen, K.; Maran, F. $Au_{25}(SEt)_{18}$, a Nearly Naked Thiolate-Protected Au_{25} Cluster Structural Analysis by Single Crystal X-ray Crystallography and Electron Nuclear Double Resonance. *ACS Nano* **2014**, *8*, 3904−3912.
(101) Yang, H.; Wang, Y.; Huang, H.; Gell, L.; Lehtovaara, L.; Malola, S.; Häkkinen, H.; Zheng, N. All-Thiol-Stabilized Ag_{44} and $Au_{12}Ag_{32}$ Nanoparticles with Single-Crystal Structures. *Nat. Commun.* **2013**, *4*, 2422.
(102) Li, Y.; Juarez-Mosqueda, R.; Song, Y.; Zhang, Y.; Chai, J.; Mpourmpakis, G.; Jin, R. Ligand Exchange on $Au_{38}(SR)_{24}$: Substituent Site Effects of Aromatic Thiols. *Nanoscale* **2020**, *12*, 9423−9429.
(103) Gan, Z.; Chen, J.; Wang, J.; Wang, C.; Li, M.-B.; Yao, C.; Zhuang, S.; Xu, A.; Li, L.; Wu, Z. The Fourth Crystallographic Closest Packing Unveiled in the Gold Nanocluster Crystal. *Nat. Commun.* **2017**, *8*, 14739.
(104) Gan, Z.; Chen, J.; Liao, L.; Zhang, H.; Wu, Z. Surface Single-Atom Tailoring of a Gold Nanoparticle. *J. Phys. Chem. Lett.* **2018**, *9*, 204−208.
(105) Talapin, D. V.; Shevchenko, E. V.; Kornowski, A.; Gaponik, N.; Haase, M.; Rogach, A. L.; Weller, H. A New Approach to Crystallization of CdSe Nanopartilces into Ordered Three-Dimensional Superlattices. *Adv. Mater.* **2001**, *13*, 1868−1871.
(106) Zhang, C.; Macfarlane, R. J.; Young, K. L.; Choi, C. H.; Hao, L.; Auyeung, E.; Liu, G.; Zhou, X.; Mirkin, C. A. A General Approach to DNA-Programmable Atom Equivalents. *Nat. Mater.* **2013**, *12*, 741−746.
(107) Wang, S.; Yao, H.; Sato, S.; Kimura, K. Inclusion-Water-Cluster in a Three-Dimensional Superlattice of Gold Nanoparticles. *J. Am. Chem. Soc.* **2004**, *126*, 7438−7439.
(108) Sun, Z.; Ni, W.; Yang, Z.; Kou, X.; Li, L.; Wang, J. pH-Controlled Reversible Assembly and Disassembly of Gold Nanorods. *Small* **2008**, *4*, 1287−1292.
(109) Jang, S. G.; Kramer, E. J.; Hawker, C. J. Controlled Supramolecular Assembly of Micelle-Like Gold Nanoparticles in PS-*b*-P2VP Diblock Copolymers via Hydrogen Bonding. *J. Am. Chem. Soc.* **2011**, *133*, 16986−16996.
(110) Ni, W.; Mosquera, R. A.; Pérez-Juste, J.; Liz-Marzán, L. M. Evidence for Hydrogen-Bonding-Directed Assembly of Gold Nanorods in Aqueous Solution. *J. Phys. Chem. Lett.* **2010**, *1*, 1181−1185.
(111) Salorinne, K.; Malola, S.; Wong, O. A.; Rithner, C.; Chen, X.; Ackerson, C. J.; Häkkinen, H. Conformation and Dynamics of the Ligand Shell of a Water-Soluble Au_{102} Nanoparticle. *Nat. Commun.* **2016**, *7*, 10401.
(112) Nonappa; Lahtinen, T.; Haataja, J. S.; Tero, T.-R.; Häkkinen, H.; Ikkala, O. Template-Free Supracolloidal Self-Assembly of Atomically PreciseGold Nanoclusters From 2D Colloidal Crystals to Spherical Capsids. *Angew. Chem., Int. Ed.* **2016**, *55*, 16035−16038.
(113) Som, A.; Chakraborty, I.; Maark, T. A.; Bhat, S.; Pradeep, T. Cluster-Mediated Crossed Bilayer Precision Assemblies of 1D Nanowires. *Adv. Mater.* **2016**, *28*, 2827−2833.
(114) Chakraborty, A.; Fernandez, A. C.; Som, A.; Mondal, B.; Natarajan, G.; Paramasivam, G.; Lahtinen, T.; Häkkinen, H.; Nonappa; Pradeep, T. Atomically Precise Nanocluster Assemblies Encapsulating Plasmonic Gold Nanorods. *Angew. Chem.* **2018**, *130*, 6632−6636.
(115) AbdulHalim, L. G.; Ashraf, S.; Katsiev, K.; Kirmani, A. R.; Kothalawala, N.; Anjum, D. H.; Abbas, S.; Amassian, A.; Stellacci, F.; Dass, A.; Hussain, I.; Bakr, O. M. A Scalable Synthesis of Highly Stable and Water Dispersible $Ag_{44}(SR)_{30}$ Nanoclusters. *J. Mater. Chem. A* **2013**, *1*, 10148−10154.
(116) Desireddy, A.; Conn, B. E.; Guo, J.; Yoon, B.; Barnett, R. N.; Monahan, B. M.; Kirschbaum, K.; Griffith, W. P.; Whetten, R. L.; Landman, U.; Bigioni, T. P. Ultrastable Silver Nanoparticles. *Nature* **2013**, *501*, 399−402.
(117) Yoon, B.; Luedtke, W. D.; Barnett, R. N.; Gao, J.; Desireddy, A.; Conn, B. E.; Bigioni, T. P.; Landman, U. Hydrogen-Bonded Structure and Mechanical Chiral Response of a Silver Nanoparticle Superlattice. *Nat. Mater.* **2014**, *13*, 807−811.
(118) Correa-Duarte, M. A.; Pérez-Juste, J.; Sánchez-Iglesias, A.; Giersig, M.; Liz-Marzán, L. M. Aligning Au Nanorods by Using Carbon Nanotubes as Templates. *Angew. Chem., Int. Ed.* **2005**, *44*, 4375−4378.
(119) Georgakilas, V.; Gournis, D.; Tzitzios, V.; Pasquato, L.; Guldi, D. M.; Prato, M. Decorating Carbon Nanotubes with Metal or Semiconductor Nanoparticles. *J. Mater. Chem.* **2007**, *17*, 2679−2694.
(120) Shevchenko, E. V.; Talapin, D. V.; Kotov, N. A.; O'Brien, S.; Murray, C. B. Structural Diversity in Binary Aanoparticle Superlattices. *Nature* **2006**, *439*, 55−59.
(121) Shevchenko, E. V.; Talapin, D. V.; Murray, C. B.; O'Brien, S. Structural Characterization of Self-Assembled Multifunctional Binary Nanoparticle Superlattices. *J. Am. Chem. Soc.* **2006**, *128*, 3620−3637.
(122) Chen, Z.; Moore, J.; Radtke, G.; Sirringhaus, H.; O'Brien, S. Binary Nanoparticle Superlattices in the Semiconductor-Semiconductor System: CdTe and CdSe. *J. Am. Chem. Soc.* **2007**, *129*, 15702−15709.
(123) Smith, D. K.; Goodfellow, B.; Smilgies, D.-M.; Korgel, B. A. Self-Assembled Simple Hexagonal AB_2 Binary Nanocrystal Superlattices: SEM, GISAXS, and Defects. *J. Am. Chem. Soc.* **2009**, *131*, 3281−3290.
(124) Eldridge, M. D.; Madden, P. A.; Frenkel, D. Entropy-Driven Formation of a Superlattice in a Hard-Sphere Binary Mixture. *Nature* **1993**, *365*, 35−37.
(125) Xia, Y.; Nguyen, T. D.; Yang, M.; Lee, B.; Santos, A.; Podsiadlo, P.; Tang, Z.; Glotzer, S. C.; Kotov, N. A. Self-Assembly of

https://dx.doi.org/10.1021/jacs.0c05866
J. Am. Chem. Soc. 2020, 142, 13627−13644

Self-Limiting Monodisperse Supraparticles from Polydisperse Nanoparticles. *Nat. Nanotechnol.* **2012**, *7*, 479−479.
(126) Kostiainen, M. A.; Hiekkataipale, P.; Laiho, A.; Lemieux, V.; Seitsonen, J.; Ruokolainen, J.; Ceci, P. Electrostatic Assembly of Binary Nanoparticle Superlattices Using Protein Cages. *Nat. Nanotechnol.* **2013**, *8*, 52−56.
(127) Tang, Z.; Kotov, N. A.; Giersig, M. Spontaneous Organization of Single CdTe Nanoparticles into Luminescent Nanowires. *Science* **2002**, *297*, 237−240.
(128) Yan, J.; Malola, S.; Hu, C.; Peng, J.; Dittrich, B.; Teo, B. K.; Häkkinen, H.; Zheng, L.; Zheng, N. Co-Crystallization of Atomically Precise Metal Nanoparticles Driven by Magic Atomic and Electronic Shells. *Nat. Commun.* **2018**, *9*, 3357.
(129) He, L.; Gan, Z.; Xia, N.; Liao, L.; Wu, Z. Alternative Array Stacking of $Ag_{26}Au$ and $Ag_{24}Au$ Nanoclusters. *Angew. Chem., Int. Ed.* **2019**, *58*, 9897−9901.
(130) Rosi, N. L.; Mirkin, C. A. Nanostructures in Biodiagnostics. *Chem. Rev.* **2005**, *105*, 1547−1562.
(131) Rana, S.; Bajaj, A.; Mout, R.; Rotello, V. M. Monolayer Coated Gold Nanoparticles for Delivery Applications. *Adv. Drug Delivery Rev.* **2012**, *64*, 200−216.
(132) Higaki, T.; Li, Y.; Zhao, S.; Li, Q.; Li, S.; Du, X. S.; Yang, S.; Chai, J.; Jin, R. Atomically Tailored Gold Nanoclusters for Catalytic Application. *Angew. Chem.* **2019**, *131*, 8377−8388.
(133) Zeng, C.; Weitz, A.; Withers, G.; Higaki, T.; Zhao, S.; Chen, Y.; Gil, R. R.; Hendrich, M.; Jin, R. Controlling Magnetism of $Au_{133}(TBBT)_{52}$ Nanoclusters at Single Electron Level and Implication for Nonmetal to Metal Transition. *Chem. Sci.* **2019**, *10*, 9684−9691.
(134) Aikens, C. M. Electronic and Geometric Structure, Optical Properties, and Excited State Behavior in Atomically Precise Thiolate-Stabilized Noble Metal Nanoclusters. *Acc. Chem. Res.* **2018**, *51*, 3065−3073.
(135) Xu, W. W.; Zeng, X. C.; Gao, Y. Application of Electronic Counting Rules for Ligand-Protected Gold Nanoclusters. *Acc. Chem. Res.* **2018**, *51*, 2739−2747.
(136) Pei, Y.; Wang, P.; Ma, Z.; Xiong, L. Growth-Rule-Guided Structural Exploration of Thiolate-Protected Gold Nanoclusters. *Acc. Chem. Res.* **2019**, *52*, 23−33.
(137) Taylor, M. G.; Mpourmpakis, G. Thermodynamic Stability of Ligand-protected Metal Nanoclusters. *Nat. Commun.* **2017**, *8*, 15988.
(138) Malola, S.; Kaappa, S.; Häkkinen, H. Role of Nanocrystal Symmetry in the Crossover Region from Molecular to Metallic Gold Nanoparticles. *J. Phys. Chem. C* **2019**, *123*, 20655−20663.
(139) Higaki, T.; Zhou, M.; He, G.; House, S. D.; Sfeir, M. Y.; Yang, J. C.; Jin, R. Anomalous Phonon Relaxation in $Au_{333}(SR)_{79}$ Nanoparticles with Nascent Plasmons. *Proc. Natl. Acad. Sci. U. S. A.* **2019**, *116*, 13215−13220.
(140) Zhou, M.; Higaki, T.; Hu, G.; Sfeir, M. Y.; Chen, Y.; Jiang, D.; Jin, R. Three-orders-of-magnitude Variation of Carrier Lifetimes with Crystal Phase of Gold Nanoclusters. *Science* **2019**, *364*, 279−282.
(141) Negishi, Y.; Nakazaki, T.; Malola, S.; Takano, S.; Niihori, Y.; Kurashige, W.; Yamazoe, S.; Tsukuda, T.; Häkkinen, H. A Critical Size for Emergence of Nonbulk Electronic and Geometric Structures in Dodecanethiolate-Protected Au Clusters. *J. Am. Chem. Soc.* **2015**, *137*, 1206−1212.
(142) Cook, A. W.; Hayton, T. W. Case Studies in Nanocluster Synthesis and Characterization: Challenges and Opportunities. *Acc. Chem. Res.* **2018**, *51*, 2456−2464.

https://dx.doi.org/10.1021/jacs.0c05866
J. Am. Chem. Soc. 2020, 142, 13627−13644